The XMM cluster survey: exploring scaling relations and completeness of the dark energy survey year 3 redMaPPer cluster catalogue

E. W. Upsdell [1]⋆ P. A. Giles [1]⋆ A. K. Romer,[1]⋆ R. Wilkinson,[1] D. J. Turner [1], M. Hilton,[2,3]
E. Rykoff,[4] A. Farahi,[5] S. Bhargava,[6] T. Jeltema [7] M. Klein,[8] A. Bermeo,[1] C. A. Collins,[9]
L. Ebrahimpour,[10,11] D. Hollowood,[7] R. G. Mann,[12] M. Manolopoulou,[12] C. J. Miller,[13] P. J. Rooney,[1]
Martin Sahlén,[14] J. P. Stott,[15] P. T. P. Viana,[10,11] S. Allam,[16] O. Alves,[17] D. Bacon,[18] E. Bertin,[19]
S. Bocquet,[20] D. Brooks,[21] D. L. Burke,[4,22] M. Carrasco Kind,[23,24] J. Carretero,[25] M. Costanzi,[26,27,28]
L. N. da Costa,[29] M. E. S. Pereira,[30] J. De Vicente,[31] S. Desai,[32] H. T. Diehl,[16] J. P. Dietrich,[20] S. Everett,[33]
I. Ferrero,[34] J. Frieman,[16,35] J. García-Bellido,[36] D. W. Gerdes,[37] G. Gutierrez,[16] S. R. Hinton,[38]
K. Honscheid,[39,40] D. J. James,[41] K. Kuehn,[42,43] N. Kuropatkin,[16] M. Lima,[29,44] J. L. Marshall,[45]
J. Mena-Fernández,[31] F. Menanteau,[23,24] R. Miquel,[25,46] J. J. Mohr,[20,47] R. L. C. Ogando,[48] A. Pieres,[29,48]
M. Raveri,[49] M. Rodriguez-Monroy,[31] E. Sanchez,[31] V. Scarpine,[16] I. Sevilla-Noarbe,[31] M. Smith,[50]
E. Suchyta,[51] M. E. C. Swanson, G. Tarle,[17] C. To,[39] N. Weaverdyck,[17,52] J. Weller[47,53] and P. Wiseman[50]

Affiliations are listed at the end of the paper

ABSTRACT

We cross-match and compare characteristics of galaxy clusters identified in observations from two sky surveys using two completely different techniques. One sample is optically selected from the analysis of 3 years of Dark Energy Survey observations using the redMaPPer cluster detection algorithm. The second is X-ray selected from *XMM* observations analysed by the *XMM* Cluster Survey. The samples comprise a total area of 57.4 deg², bounded by the area of four contiguous XMM survey regions that overlap the DES footprint. We find that the X-ray-selected sample is fully matched with entries in the redMaPPer catalogue, above $\lambda > 20$ and within $0.1 < z < 0.9$. Conversely, only 38 per cent of the redMaPPer catalogue is matched to an X-ray extended source. Next, using 120 optically clusters and 184 X-ray-selected clusters, we investigate the form of the X-ray luminosity–temperature ($L_X - T_X$), luminosity–richness ($L_X - \lambda$), and temperature–richness ($T_X - \lambda$) scaling relations. We find that the fitted forms of the $L_X - T_X$ relations are consistent between the two selection methods and also with other studies in the literature. However, we find tentative evidence for a steepening of the slope of the relation for low richness systems in the X-ray-selected sample. When considering the scaling of richness with X-ray properties, we again find consistency in the relations (i.e. $L_X - \lambda$ and $T_X - \lambda$) between the optical and X-ray-selected samples. This is contrary to previous similar works that find a significant increase in the scatter of the luminosity scaling relation for X-ray-selected samples compared to optically selected samples.

Key words: X-rays: galaxies: clusters – galaxies: clusters: general – galaxies: clusters: intracluster medium – galaxies: groups: general.

1 INTRODUCTION

Galaxy clusters are the most massive collapsed objects in the Universe, forming at the intersections of large-scale structure filaments and provide an ideal laboratory for cosmological studies. The formation of large-scale structure is predicated on the gravitational collapse of primordial density fluctuations and, therefore, the halo mass function (as measured by the number of clusters of mass M per unit comoving volume) is sensitive to cosmological models (e.g.

Vikhlinin et al. 2009). Probing number counts and mass can therefore place constraints on cosmology and this is particularly powerful when used in complement with other cosmological markers, such as the angular power spectrum of the cosmic microwave background (e.g. Hou et al. 2014; Planck Collaboration XXIV 2016) or baryonic acoustic oscillations (e.g. Carvalho et al. 2016).

In Abbott et al. (2020, hereafter A20), the Dark Energy Survey (hereafter DES, Dark Energy Survey Collaboration et al. 2016) collaboration released cluster cosmology results, estimated using the number density of clusters and a stacked weak lensing mass calibration. These results highlighted a significant tension between the calculated values of cosmological parameters (namely Ω_m and σ_8) versus those produced by other surveys, including other DES

analyses. The tensions in the σ_8–Ω_m plane were 1.1σ versus SPT-2500 (Bocquet et al. 2019), 1.7σ versus Weighing the Giants (Applegate et al. 2014), 2.4σ versus DES 3x2pt (Abbott et al. 2018), and 5.6σ versus Planck (Planck Collaboration XXIV 2016). A20 suggests that the tension is most likely explained by a failure in the understanding of the optical selection on the weak-lensing signal such as biases due to cluster orientation and projection effects (e.g. Wu et al. 2022). A20 notes that the tension is reduced if lower mass clusters with a richness (λ) < 30 are removed from the sample. Richness is redMaPPer's (see Section 2.1 for an introduction to redMaPPer) probabilistic measure of the number of galaxies in a cluster and is the main optical observable in the DES cluster analysis. The A20 authors point out that had the analysis been performed only on the higher mass systems, this systematic tension would not have been discovered.

It is therefore of critical importance for inferring cosmology to understand the differences at these lower richnesses/masses, either their physical properties or unknown systematics in the modelling of these systems. We therefore have two primary considerations:

(i) The completeness and purity of the catalogue used for number count analysis, particularly at lower masses

    (a) The completeness and purity of the RM sample has been confirmed at λ > 40 using the SPT galaxy cluster sample (Grandis et al. 2021). In this work, we are able to use X-ray surveys and cross-matching to the DESY3 redMaPPer optical catalogue (see Section 2.1) to probe the lower lambda redMaPPer systems.

(ii) The mass and scatter of lower mass halos

    (a) Measuring masses for individual galaxy clusters directly is inherently difficult and expensive (especially over relatively shallow survey regions) and so A20 used stacked weak-lensing data (see McClintock et al. 2018). However, in using stacked data, information about the scatter of the observable versus mass is lost. The bottom-up hierarchical formation model allows us to relate mass to more readily observable properties such as X-ray temperature and luminosity via simple power-law relations. Further, cosmological hydrodynamical simulations using first principles suggest the power-law slope and scatter may be scale-dependant (e.g. Le Brun et al. 2017; Farahi et al. 2018; Anbajagane et al. 2020). By considering the scatter and evolution of these scaling relations, we can re-introduce the lost scatter into the mass calibrations and cosmological models can be constrained.

Currently, there are no all-sky X-ray surveys to significant and consistent depth, making cross-correlation analysis between X-ray and optical studies difficult, particularly at higher redshifts and lower richnesses. We note that, in the future, eROSITA (Predehl et al. 2021), which took first light in 2019, will create and release the deepest, most detailed X-ray all-sky survey ever made having 30–50 times the sensitivity of the previous all-sky X-ray survey by ROSAT. The few studies that consider the cross-correlation between optical and X-ray surveys, either suffer from small overlapping contiguous areas (e.g. Connelly et al. 2012, <1 deg^2), use cross-matches from catalogues in non-contiguous regions (e.g. Farahi et al. 2019; Giles et al. 2022b) or use targeted X-ray follow-up of optically selected samples (e.g. Andreon et al. 2016), although again, across a non-contiguous region. The most comparable study to this one in terms of using serendipitous detections overlapping survey areas is Giles et al. (2022a), which used XXL and GAMA. However, the sample in Giles et al. (2022a)

is limited in size by the spectroscopic selection to ∼30 clusters and the sky coverage is only 14.6 deg^2.

In this paper, we overcome these shortcomings by using four contiguous fields of XMM observations, totalling 57.4 deg^2, within the DES footprint. X-ray clusters are found using analysis performed by the XMM Cluster Survey (XCS) and for the optical dataset, we use the redMaPPer cluster catalogue, derived from 3 years of DES observations. Compared to G22a who only used clusters designated as C1 in the XXL catalogue, our sample area is ≈4 times larger (57.4 deg versus 14 deg) and our cluster sample size is ≈11 times larger (341 versus 30).

The outline of the paper is as follows: In Section 2, the construction of the samples used is detailed; Section 3 outlines the overlaps of the optically selected and X-ray selected samples and explains the differences; Section 4 describes the methods used for recovering the X-ray observables and the resultant subsamples used for the scaling relations. Section 5 presents the scaling relations and the fitted results. In Section 6, we briefly discuss low signal-to-noise clusters and binning on our scaling relation results, compare our results to analogous literature works, and consider any implications for samples derived from the Legacy Survey of Space and Time (LSST). Finally, we summarize our conclusions in Section 7. Throughout this paper, we assume a cosmology of $\Omega_M = 0.3$, $\Omega_\Lambda = 0.7$, and $H_0 = 70$ km s^{-1} Mpc^{-1}.

2 SAMPLES

In this section, we describe how the optical and X-ray data were selected and combined to form the basis of the samples used throughout this work.

2.1 The surveys and catalogues

The optical data were taken from the DES, an optical survey covering approximately 5000 square degrees of the Southern sky (the DES footprint is highlighted in Fig. 1 (top), given by the red-shaded region). Observations were made using a 570 megapixel camera, DECam (Flaugher et al. 2015), made up of 62 2048 × 4096 CCDs and 12 2048 × 2048 CCDs, mounted on the 4-m *Blanco* telescope at the Cerro Tololo Inter-American Observatory in Chile. Specifically, we make use of the cluster catalogue generated by the red-sequence Matched-filter Probabilistic Percolation cluster finder algorithm[1] (hereafter redMaPPer, Rykoff et al. 2014, 2016), run on the DES Year 1–Year 3 data (hereafter DESY3, Sevilla-Noarbe et al. 2021). redMaPPer iteratively calculates photometric redshifts for probable clusters by self-training the red sequence model and assigning a characteristic richness (λ) based on the sum of the probabilities of membership for all galaxies within a scale radius, R_λ, where $R_\lambda = 1.0 \ h^{-1}$Mpc$(\lambda/100)^{0.2}$.

The XMM Cluster Survey (hereafter XCS, Romer et al. 1999) is a serendipitous survey of *XMM–Newton* observations (see Fig. 1, top-plot, black points) with the primary aim of detecting galaxy clusters. XCS pipelines process and clean all publicly available observations from the XMM Science Archive (Arviset et al. 2002), with the ultimate aim of finding galaxy clusters.

2.2 The sky regions used

In this work, we make use of four large contiguous fields that have complete X-ray coverage from *XMM*, within the DES footprint. The

---
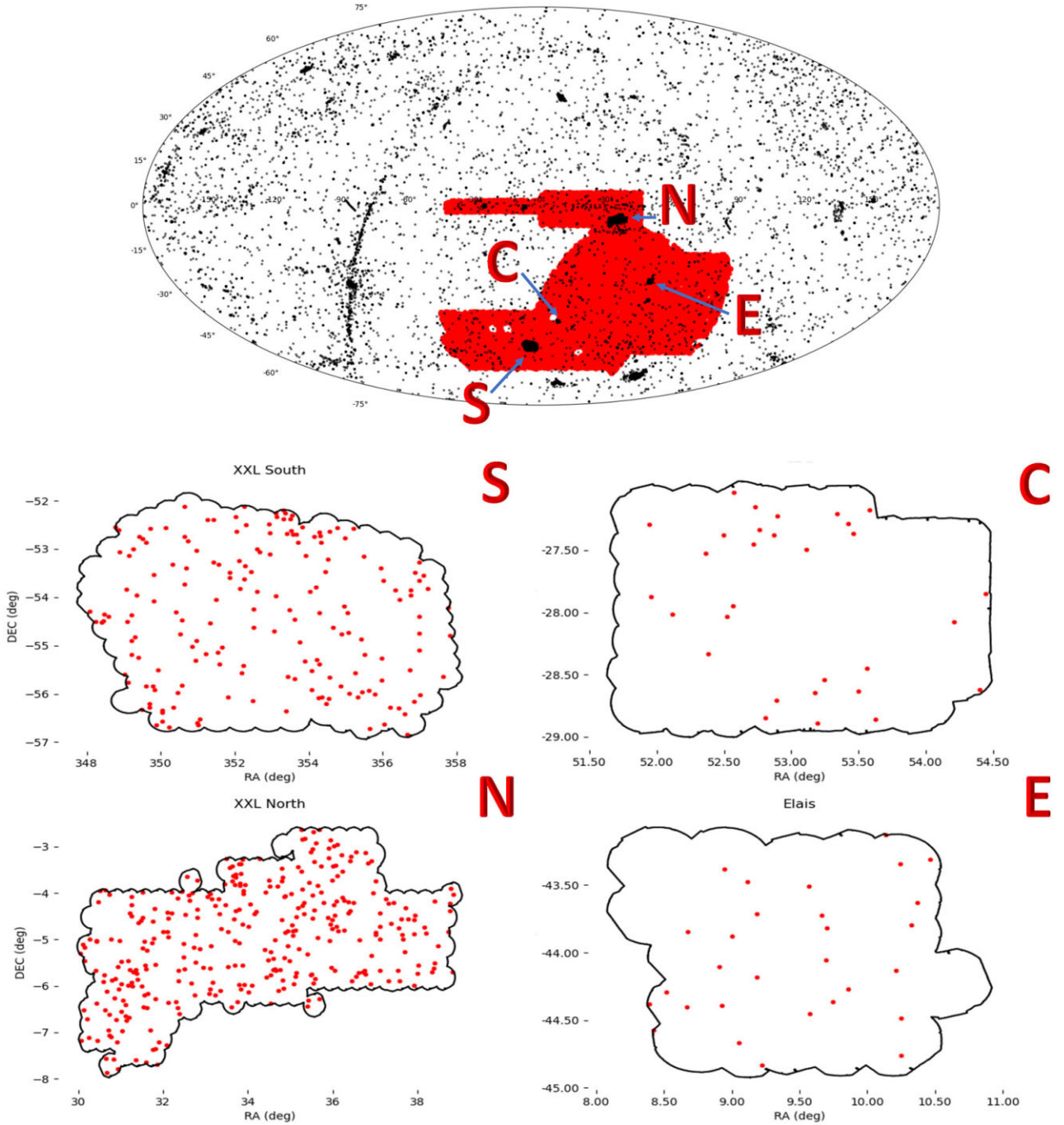
[1]Version 6.4.22 + 2_lgt5_vl50

Figure 1. (Top) XMM observations over the whole sky (black points) with the DES footprint highlighted by the red-shaded region. We highlight the survey regions used in this work, corresponding to XXL-North(N), XXL-South (S), ELAIS (E), and CDS (C). (Bottom) Outlines of the footprints covered for each of the four corresponding contiguous regions, with the red points indicating the location of redMaPPer clusters in the DES catalogue (with $\lambda > 20$ and $0.1 < z < 0.9$, see Section 2.3). Note: the four subplots are not to equal scale: N: 27 deg^2; S: 23.7 deg^2; C: 4.6 deg^2; E: 2.1 deg^2.

four regions are shown in Fig. 1. The two larger contiguous regions are the XXL$_{North}$ and XXL$_{South}$ regions (denoted as N and S in Fig. 1, respectively) that form the basis of the XXL Survey (Pierre et al. 2016). The two smaller regions, CDS and ELAIS (denoted C and E in Fig. 1, respectively), are part of the extended SERVS survey (Mauduit et al. 2012). Within the outline of the footprints in Fig. 1, the location of redMaPPer cluster detections with $\lambda > 20$ are given by the red points (see Section 2.3). Details of the regions are outlined in Table 1. In total, the regions constitute 57.4 deg^2 of contiguous

overlap between the DES and XCS observations, although it is noted that the median X-ray exposure times at the redMaPPer cluster locations within the survey regions are 3 times greater in CDS and ELAIS than in XXL.

2.3 The optical sample

Within the 57.4 deg^2 of the four contiguous regions, the full redMaPPer catalogue ($\lambda > 5$) contains 9792 entries. We designate

Table 1. The four contiguous regions comprised of *XMM* observations falling within the DES footprint (see Fig. 1). Median exposure time is given for all clusters at the redMaPPer location.

Region	Area (deg^2)	RM clusters ($\lambda >20$)	XMM observations	RM density (clusters deg^{-2})	Median X-ray exposure Time (ks)
N-XXL$_{North}$	27	337	375	11.5	10.8
S-XXL$_{South}$	23.7	180	276	7.6	8.7
C-CDS	4.6	30	107	6.5	30
E-ELAIS	2.1	29	37	9.5	28

this sample set as RM$_{all}$ and use this sample when considering the completeness of the X-ray-selected sample (see Section 3). For the purpose of creating the optical sample used to derive scaling relations (see Section 4), we cut this catalogue by both richness and redshift. First, we set a minimum λ limit of 20 for two reasons:

(i) to be consistent with the DES cluster cosmology analysis (Abbott et al. 2018);

(ii) it is likely that only a small fraction of $\lambda <20$ clusters would be detected in our current X-ray data, leading to a large amount of incompleteness (especially at high redshifts, see Section 3).

This results in a subsample of 576 cluster entries. We then make a further cut to confine the redshift range as $0.1 < z < 0.9$. This leaves a final redMaPPer optical candidate list of 469 potential clusters, which we designate as RM$_{cut}$.

We then use XCS's image processing suite OCTAVIUS (**O**bject **C**lassification **T**ools for **A**stronomy Images and **VI**s**U**ali**S**ation) to confirm, or otherwise, the presence of an XCS extended source in the corresponding XMM observation. The process is similar to that as undertaken in Giles et al. (2022b, hereafter G22b). Briefly, we matched each redMaPPer cluster to its nearest XCS X-ray counterpart within 2 h^{-1} Mpc (based on the redMaPPer redshift). This was chosen to encapsulate the entire range of mis-centering between redMaPPer and XAPA centroids (see Zhang et al. 2019). Each potential match is visually inspected to confirm whether the XCS extended source is likely physically associated with the redMaPPer cluster in question (see Appendix A for examples). After visual inspection, 178 redMaPPer clusters are retained for having a viable counterpart in the XCS catalogue. We designate the sample of 178 confirmed redMaPPer clusters as RM$_{XCS}$. The remaining 291 redMaPPer clusters are unmatched to an X-ray extended source. These are discussed further in Section 3.3.

2.4 The X-ray sample

The original X-ray data reduction process is fully described in Lloyd-Davies et al. (2011, hereafter LD11), with updates described by G22b. Briefly, the data were processed using XMM-SAS version 14.0.0 and event lists generated using the EPCHAIN and EMCHAIN tools. Periods of high background levels and particle contamination were excluded using an iterative 3σ clipping process performed on the light curves with time bins falling outside this range excluded. Single camera (i.e. PN, MOS1, and MOS2) images and exposure maps were then generated from the cleaned events files, spatially binned with a pixel size of 4.35 arcsec. The images and exposure maps were extracted in the 0.5–2.0 keV band, with individual camera images and exposure maps merged to create a single image per XMM observation.

Following reduction, the resultant images are run through the XCS source detection routine, the XCS Automated Pipeline Algorithm (XAPA, see LD11), based upon a bespoke WAVDETECT (Freeman et al. 2002) analysis, to detect both point-like and extended sources.

XAPA collates unique entries into a Master Source List (MSL), which is our starting X-ray detection catalogue. Over the 57.4 deg^2 of the four contiguous regions, there are 25 213 sources in the MSL, of which 1987 are classified as extended sources. When a large extended source is found across multiple XMM observations, XAPA can accidentally identify the same cluster twice as distinct objects. We remove these duplicates leaving 1972 extended sources, which we designate as the XCS$_{ext}$ sample. Using OCTAVIUS, we visually inspect each X-ray extended source against its corresponding contrast-enhanced DES image to confirm the presence of an overabundance of red galaxies (see Appendix A for image examples). Following this visual inspection process, we produce a list of 341 clusters that are X-ray selected and optically confirmed. We designate this sample XCS$_{opt}$. Although XCS$_{opt}$ represents only 17 per cent of the 1972 extended candidates, XAPA classifies many point spread function-sized detections as extended sources when they are often AGN. Hence, all classifications are visually inspected.

3 CROSS-MATCHING THE REDMAPPER AND XCS SAMPLES

In this section, we investigate the overlap of the optical and X-ray selected samples described in Sections 2.3 and 2.4. In Sections 3.1 and 3.2, we consider how much of the redMaPPer catalogue is covered by the XCS catalogue and vice versa. We discuss potential unmatched clusters in Section 3.3.

3.1 X-ray to optical matching

As shown in Section 2.3, there are 469 clusters in the RM$_{cut}$ sample, but only 178 in the RM$_{XCS}$ subsample. We find 38 per cent of the RM$_{cut}$ sample (see Section 2.3) are matched to an X-ray counterpart. The main driver in finding an X-ray cluster detection is the cluster's X-ray flux (and additionally on the distribution of that flux). We therefore investigate two properties of a cluster that have a bearing on the cluster flux, namely the richness (as a proxy for mass) and redshift. Additionally, we investigate the effective exposure time of the observation. Effective exposure time is calculated by adjusting raw exposure time with correction factors including telescope's effective area, field of view, and background radiation to accurately measure the amount of X-ray photons collected and decreases as a function of off-axis position on the *XMM* detector. Since the clusters can fall anywhere on the detector due to the survey nature of the observations, the effective exposure time is a property of interest to explore. One can assume that in most cases higher richnesses, lower redshifts, and greater exposure times will all increase the likelihood of detection. Fig. 2 highlights these distributions through histograms of richness (top plot), redshift (middle plot), and exposure time (bottom plot). We note the wide range of exposure times despite these being survey regions, which is due to three reasons: (i) although smaller than the XXL regions, the CDS and ELAIS regions are about 3 times deeper (based on median exposures, see Table 1), (ii) the off-
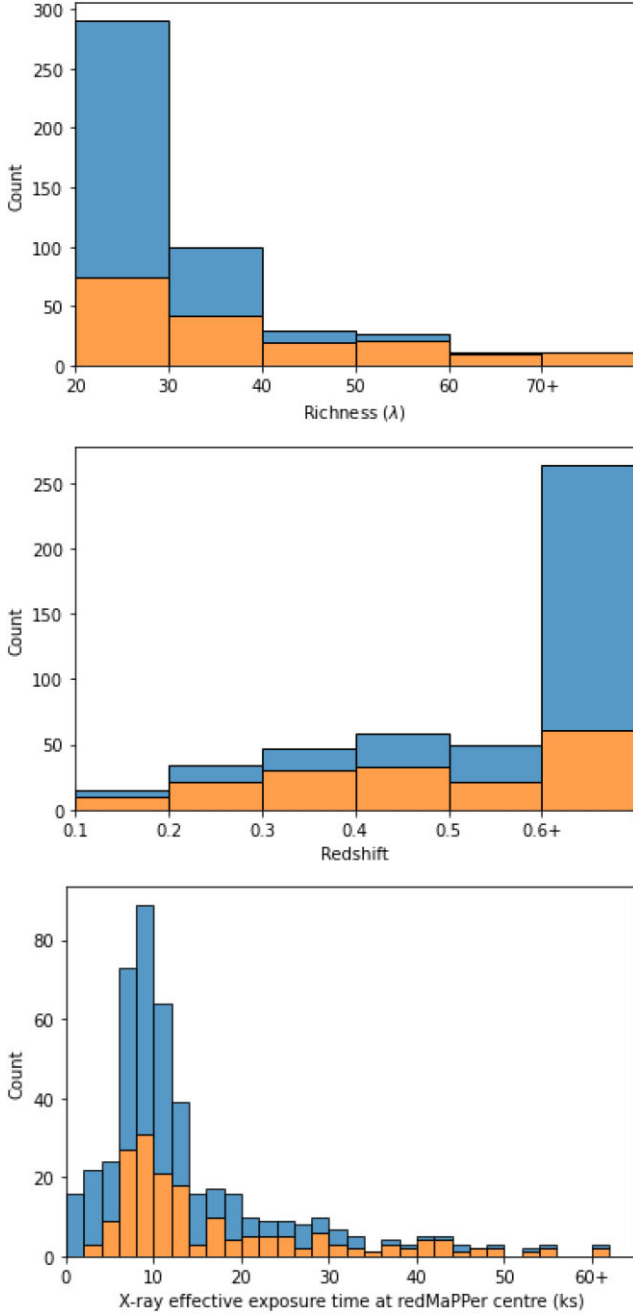
Figure 2. Stacked histograms of redMaPPer clusters with (orange) and without (blue) an X-ray counterpart as a function of Richness (Top), Redshift (Middle), and *XMM* effective exposure time (Bottom).

Figure 3. Composite mosaic of the exposure maps of *XMM* observations in the XXL_south region. Brighter areas show regions with multiple exposures.

Figure 4. (Redshift versus Richness scatter distribution for confirmed (orange) and unconfirmed (blue) clusters. Size of bubble relates to observation exposure time – larger = longer.

We explore further whether these properties are intrinsically linked in terms of the likelihood of detection. As shown in Fig. 4, there is a large number of high redshift clusters with short exposure observations at these lower richnesses. This observation correlates with the expectation from the cluster mass function that we should see a greater number of lower mass clusters, but our current X-ray surveys are not sensitive enough to detect them across the full DES redMaPPer redshift range.

3.2 Optical to X-ray matching

While we have shown that the X-ray selected sample does indeed suffer from a low level of matches with the optical sample (especially at low richnesses and high redshifts), it is also necessary to confirm whether the redMaPPer catalogue detects all known X-ray clusters. To do this, we consider the X-ray sample XCS_opt (see Section 2.4), which is the sample of X-ray extended sources with a visually confirmed overabundance of red galaxies in the DES imagery. As there are no redshift or richness values associated with this X-ray data set, we use redMaPPer in 'scanning mode' to probe them. In

axis location of the serendipitously detected clusters, and (iii) there have been a number of specific deep observations outside of the original surveys as illustrated by the example mosaic exposure map of XXL_south shown in Fig. 3.

As expected, the trends clearly show that as a function of decreasing richness, increasing redshift, and decreasing exposure time, the cross-match success of the sample is reduced. NInety-five per cent of redMaPPer clusters with a λ above 60 are matched to an X-ray source (22 clusters) and all redMaPPer clusters with $\lambda > 70$ are recovered, although we note this complete sample is small (only 11 clusters). In contrast, for $\lambda < 30$, only 25 per cent of redMaPPer clusters have a corresponding X-ray detection.
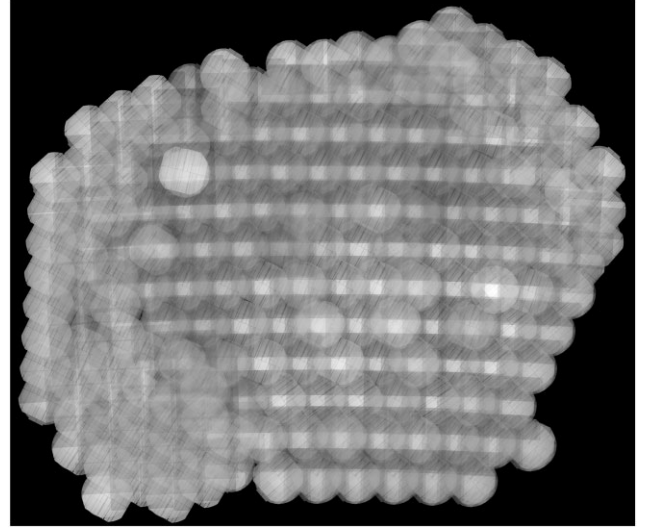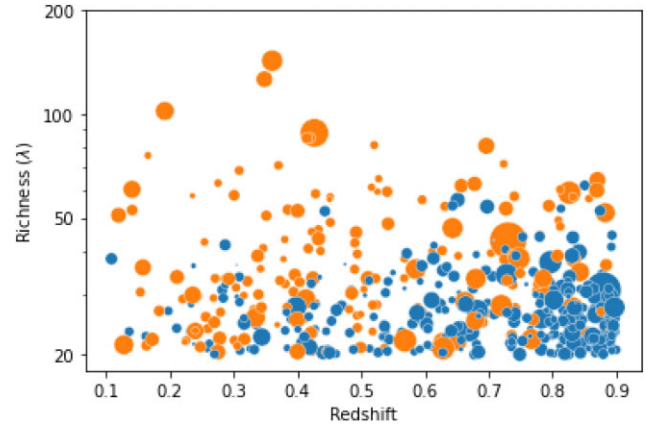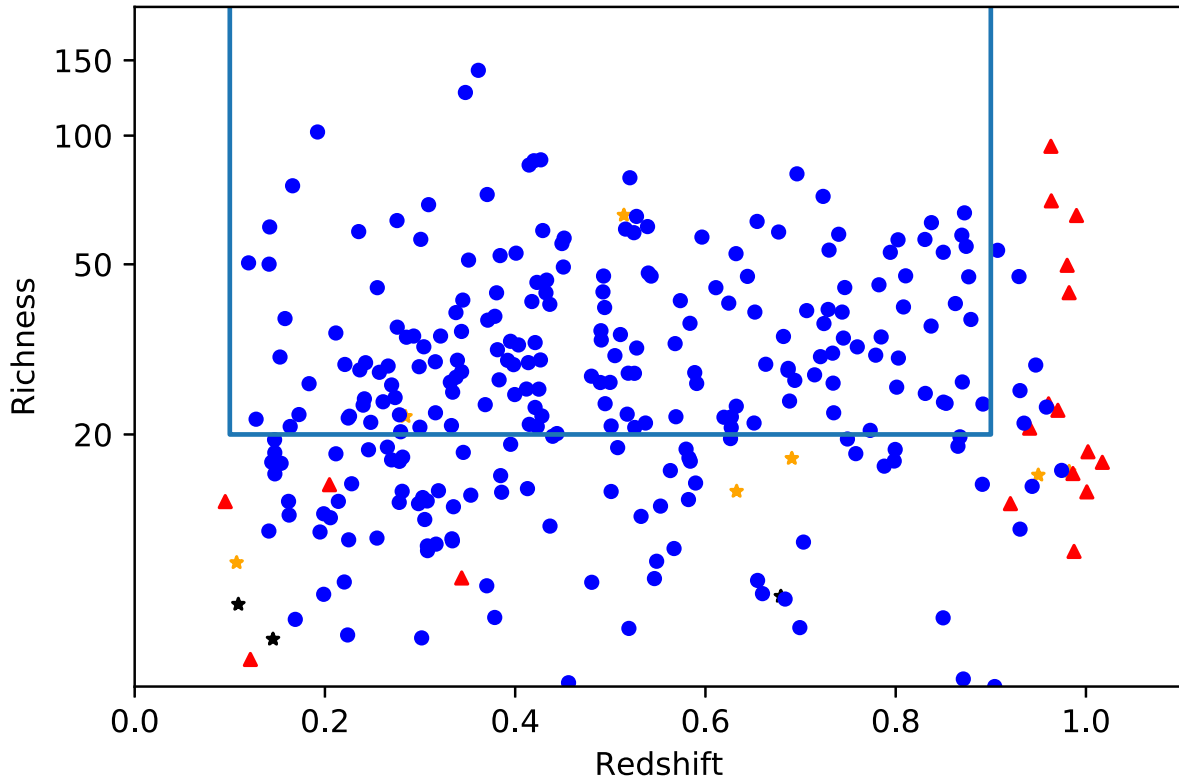
Figure 5. The distribution of redshift and richness of the 310 clusters in the X-ray-selected cluster sample (see Section 3.2). The values were determined using redMaPPer in scanning mode at the position of the XAPA centroid. Blue dots also have a counterpart in the optically selected cluster sample (see Section 2.3) with consistent redshift and richness values (i.e. (1) the distance modulus of the centres is <3 arcmin, (2) the richness modulus is <30 per cent, and (3) the redshift modulus is <10 per cent). Orange (Black) stars indicate clusters that also have a counterpart, but the richness (redshift) values are inconsistent. Red triangles indicate clusters that only appear in the X-ray-selected sample. The blue box bounds the parameter constraints placed on the RM$_{XCS}$ sample ($\lambda > 20$ and $0.1 < z < 0.9$).

'scanning mode', redMaPPer takes the position of the X-ray centroid as a prior and determines the likelihood of there being a cluster at a grid of redshifts within a projected distance of $500h^{-1}$ kpc. It then considers the maximum likelihoods and returns a redshift and richness property for each cluster, if one is found. Of the 341 scanned X-ray clusters, 31 lie in sky regions that have been masked out in DES. Regions are masked out of DES images for reasons such as a bright star or a CCD artefact that renders the area unusable for scientific analysis. redMaPPer returns a mask fraction (MASKFRAC) for each sky location that shows how much of the 500kpc region is affected. We ignore any entry that has a MASKFRAC greater than 20 per cent and these are therefore removed from further analysis. Of the remaining 310 clusters:

(i) Using the default parameters of $\lambda > 20$ and $0.1 < z < 0.9$, the 177 clusters from the RM$_{XCS}$ sample are directly matched. (The reason this is not the full 178 clusters from the RM$_{XCS}$ sample is because redMaPPer optically detects 2 clusters along the line of sight at 2 different redshifts, whereas XCS only catalogues 1 X-ray extended source at this location).

(ii) Expanding the parameter space to be unconstrained, we use the `kdtree` algorithm from Python's `scikitlearn` module to find closest neighbours between the redMaPPer-scanned X-ray centres and redMaPPer catalogue entries that fulfil the following criteria: (1) the distance between the centres is <3 arcmin; (2) the richness difference is <30 per cent; and (3) the redshift difference is <10 per cent. Thus, a further 94 clusters are directly matched.

This leaves 39 X-ray cluster candidates without a direct match in the redMaPPer catalogue based on the conditions above. Of these remaining candidates:

(i) Likely matches

    (a) Seven pairs agree on location and redshift but have a λ difference greater than 30 per cent between the scan and the catalogue

    (b) Three pairs agree on location and λ but have a redshift difference greater than 10 per cent between the scan and the catalogue

(ii) Do not match

    (a) 13 high redshift systems ($z > 0.92$) found in the scan are not in the redMaPPer catalogue (see Appendix A for images)

    (b) Eleven sources were not found by the redMaPPer scan, i.e. redMaPPer cannot determine a cluster's presence and therefore returns null values for richness and redshift. Visual inspection suggests these sources are likely high redshift and thus outside the functioning limits of redMaPPer. (See Appendix A for image examples.)

    (c) Four clusters found in the scan are not in the redMaPPer catalogue. They are low richness ($\lambda = 5.95$, 9.23, 15.26, and 13.93) systems across a wide range of redshifts ($z = 0.09$ to $z = 0.34$).

Fig. 5 shows these results as scatter points within the redshift/richness parameter space. The blue box bounds the parameter

constraints placed on the RM$_{XCS}$ sample and all matched clusters are highlighted in blue. The unmatched clusters are shown in red and clusters that match on location but with a difference in redshift or richness are shown as black and orange dots, respectively.

We can therefore state that, based on the matching process outlined above, the redMaPPer Y3 catalogue is fully matched to the XCS catalogue above $\lambda > 20$ and within $0.1 < z < 0.9$ (i.e. the redMaPPer catalogue recovers all X-ray clusters within these limits).

3.3 redMaPPer clusters undetected in X-ray observations

In this section, we investigate further why there are 291 redMaPPer clusters, with $\lambda > 20$, undetected by the current X-ray observations (see Section 2.3). We do this by comparing the required *XMM* exposure time needed to achieve a minimum of 20 counts and a signal-to-noise (SNR) ratio of at least 3, versus the actual exposure times of the observations used. We note that, for this exploratory test, we are only assuming the use of the PN camera (to match estimates of the SNR of the detected cluster, see Section 6.1.2). These SNR and count values were chosen as a cut-off because 85 per cent of the detected redMaPPer clusters (i.e. the RM$_{XCS}$ sample) have an SNR>3 (see Section 6.1.2) and 85 per cent had at least 20 PN counts. However, in running the analysis below, it became clear that, for this sample, the count criteria are dominant as the SNR was always greater than 3. (Hereafter, 'SNR>3 and counts>20' are referred to as 'the detection criteria'). To estimate the required exposure time for each cluster, we use the following process: we estimated the X-ray luminosity based upon the redMaPPer-measured λ, using the best-fitting luminosity–λ relation for the RM$_{scaling}$ sample including Upper Limits presented in Section 5.2.2 (note, for this test, we ignore the uncertainties on the relation). Using the redMaPPer determined redshift, this luminosity is converted into an expected flux. Then, using the HEASARC PIMMS[2] software and assuming an APEC model, with the same parameters we use in Section 4.1, we convert the flux into an *XMM* PN count rate assuming the redMaPPer redshift and a temperature estimated from the best-fitting temperature–richness relation given in Section 5.2.2 (again using the input λ values). To account for the background, we use the existing *XMM* observations and determined the background rate within an annulus $1.05–1.5 \times r_{500}$ centred on the redMaPPer centroid in order to be consistent with the X-ray analysis methods used throughout this paper. Values of r_{500} were estimated assuming equation (1), with the temperature estimated again from the best-fitting temperature–λ relation. (We were unable to estimate a reliable background for 15 clusters due to their close proximity to the edge of the field-of-view.) Finally, we estimated the required minimum exposure time (Exp$_{req}$) needed to 'detect' the cluster whilst fulfilling the above detection criteria.

In order to determine whether a cluster is considered 'detectable', we subtract the estimated required exposure times from the effective exposure time of the *XMM* observation, Exp$_{eff}$ (estimated at the location of the redMaPPer cluster and assuming an average exposure within the r_{500} region). Fig. 6 shows the distribution of these time differences, with red bars indicating clusters with observations that should be long enough to detect them (i.e. Exp$_{req}$<Exp$_{eff}$); green bars indicate those clusters with observations that were not long enough to detect the respective clusters. For example, if an estimated exposure time of 15 ks is required to meet the detection criteria but the existing exposure time of the XMM observation at that location was only 10 ks, it would appear in the +5ks bar (as a green bar in the distribution).
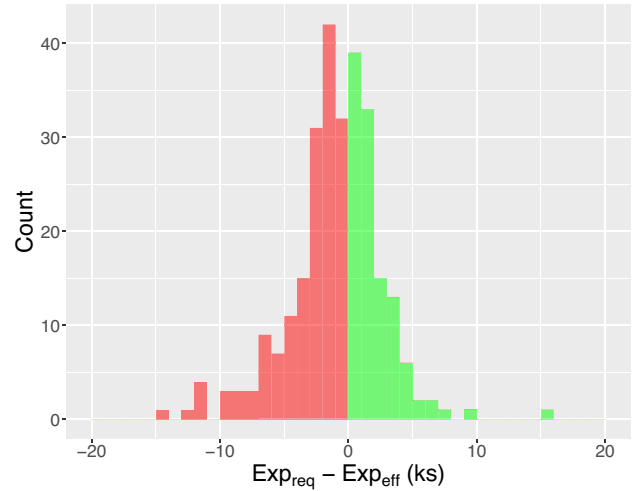
Figure 6. Histogram showing the distribution of how many extra seconds of exposure time would be required to detect a minimum of 20 PN counts with a SNR > 3 for the 276 redMaPPer clusters with a retrieved background estimate that are not confirmed by X-ray (see Section 3.3). Red bars to the left of zero indicate the 163 clusters with a current effective exposure time long enough to meet the same detection criteria assuming our best-fitting Luminosity–λ (including Upper Limits) scaling relation and background estimates. Green bars to the right show the extra time in ks that would be required to fulfil the same criteria for the remaining 113 clusters based on our best-fitting scaling relations and with background estimates taken from the respective *XMM* observation.

Based upon this analysis, there are 113 clusters ($\approx$43 per cent) in Fig. 6 where the actual observation exposure times are not sufficient to fulfil the detection criteria, and we would not expect to detect them. Conversely, there are 163 clusters where the current exposure times should be sufficient to detect a cluster. Therefore, we need to explore whether not detecting these clusters is a concern.

One reasonable explanation is that these undetected clusters are less luminous for their given richness than the luminosities estimated from the best-fitting scaling relation. This is plausible given the detected clusters used to generate the best-fitting luminosity–λ relation show significant scatter around the mean. Therefore, we shifted the scaling relation best-fitting line to the 1σ, 2σ, and 3σ scatter boundaries and re-ran the above analysis for each to show how many clusters would become undetectable if their luminosity was at each scatter band. The distributions are illustrated in Fig. 7. As shown, moving through the sigma channels, more clusters become undetectable and at the 3σ limit all but one cluster are undetectable. On visual inspection, although the X-ray emission appears to be extended, this cluster is classified as a point source by XAPA. The cluster falls very close to a PN chip gap and visually has a peaked emission profile, possibly leading to the point source classification by XAPA.

Thus, using the method outlined in this section, we have shown it is plausible that all 158 redMaPPer clusters that are deemed 'detectable' (when assuming the best-fitting scaling relation and available X-ray observations) but were not detected in the *XMM* X-ray observations become 'undetectable' within 3σ of this best-fitting scaling relation. Therefore we should not be concerned at failing to detect these clusters given the observation exposure times available to us. It should be noted that we cannot rule out the possibility that the redMaPPer richness values may be overestimated, which would, via the scaling relation, infer a higher than actual X-ray luminosity for a cluster. It is clear that deeper X-ray data are needed for a complete
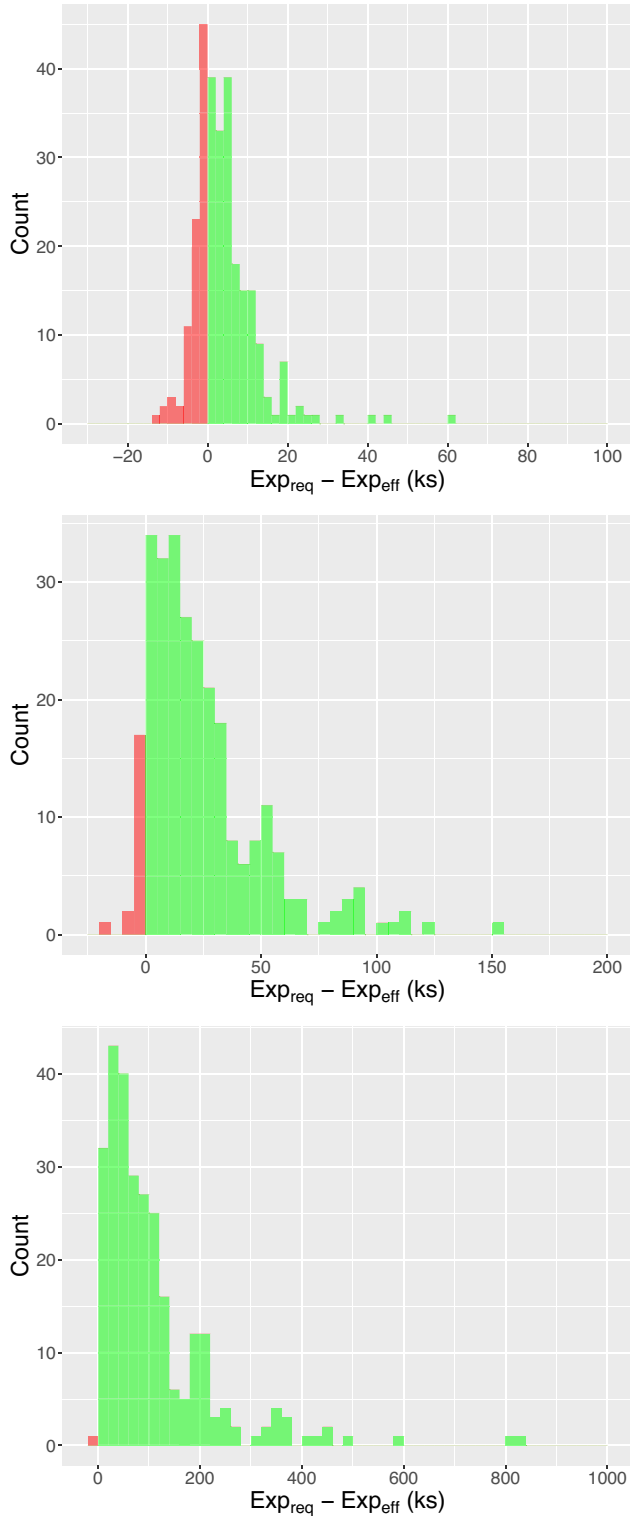
Figure 7. As per Fig. 6 but with the scaling relation, best-fitting line moved to the 1σ (top), 2σ (middle), and 3σ (bottom) channel boundaries. Using the 1σ channel, 88 clusters remain 'detectable', for the 2σ channel, 20 clusters remain 'detectable', and within the 3σ channel only 1 cluster should be 'detectable', and this is explained in Section 3.3.

sample of clusters (including the current non-detections), along with a well-understood selection function, to truly understand both the completeness and properties of redMaPPer selected clusters.

4 X-RAY ANALYSIS

4.1 Recovering X-ray temperature and luminosities

We use the XCS Post Processing Pipeline (XCS3P) to extract X-ray temperatures and luminosities from XMM observations. A detailed description of XCS3P can be found in LD11, with recent improvements described in G22b. A brief overview of the process is detailed below.

Cluster spectra are extracted using the SAS tool EVSELECT. Spectra are extracted within an iteratively determined radius of r_{500}[3] (see section 3.1.1 of G22b). Using the relation given in Arnaud, Pointecouteau & Pratt (2005), r_{500} is estimated from the X-ray temperature (T_X), using the equation:

$$E(z)r_\Delta = B_\Delta \left(\frac{T_X}{5 \text{ keV}} \right)^\beta ,\tag{1}$$

where $E(z) = \sqrt{\Omega_M(1+z)^3 + \Omega_\Lambda}$. For r_{500}, $B_{500} = 1104$ kpc and $\beta = 0.57$. Iterations are performed until r_{500} converges to within 10 per cent of the previous iteration, with a minimum requirement of three iterations. If no convergence is achieved after 10 iterations, the process is stopped and no X-ray properties are obtained.

XSPEC (Arnaud 1996) is used to fit the spectrum with an absorbed APEC (Smith et al. 2001) model, accounting for the elemental lines in the hot diffuse gas. The absorption is taken into account with a multiplicative Tbabs model (Wilms, Allen & McCray 2000), with the absorption (nH) fixed at a value estimated from HI4PI Collaboration et al. (2016), determined at the coordinates of the cluster. XSPEC fits are performed in the 0.3–7.9 keV band using a fixed abundance of $0.3 Z_\odot$ (as the typical value for the intracluster medium used in the relevant literature e.g. Kravtsov & Borgani 2012) and the redshifts are as per the RM scan. Note, we do not assign any uncertainties to the redshift as these are insignificant in the fit (the typical error on the redMaPPer photometric redshift is ≈1 per cent). The APEC temperature (T_X) and normalization are then free to vary to find the best fit. Finally, luminosities (L_X) are estimated using the XSPEC LUMIN command in both the bolometric ($L_{X, bol}$) and soft (0.5–2.0 keV) bands ($L_{X, 52}$). While we include the enhancements as detailed in G22b, we note here a further change used in this analysis. The binning of spectra for use in the XSPEC fits performed above uses the ftgrouppha command (as opposed to grppha used in XCS3P), with the 'optimized binning' parameter.[4]

4.2 Samples used for recovering temperatures and luminosities

4.2.1 The optical sample

Starting with the RM$_{XCS}$ sample (see Section 2.3) and using the process outlined above, XCS3P recovered 135 temperatures and luminosities. Of the 43 clusters that failed to return T_X or L_X values, 27 failed during the iteration process before the required minimum three iterations completed; a further 16 failed to converge after 10 iterations. Additionally, we removed clusters where the average

---

[3]r_{500} is the radius at which the density of the cluster is 500 times the critical density of the Universe

[4]Following private communication with K.Arnaud, author of XSPEC

T_X errors bars were greater than 50 per cent of the central value (removing a further 12). We also removed three clusters that had a coefficient of variation >0.5 where the coefficient of variation is defined as the ratio of the standard deviation to the mean. The final sample used for fitting the scaling relations is 120 clusters, designated as the $RM_{scaling}$ sample.

4.2.2 The X-ray sample

We use the XCS_{opt} sample of 341 clusters (Section 2.4) but remove the 27 clusters for which redMaPPer was unable to assign a redshift. We therefore pass 314 clusters to the XCS3P pipeline. Using the process outlined above, XCS3P recovers 239 temperatures and luminosities. For the 75 clusters that failed to return T_X or L_X values, 59 failed during the iteration process before the required minimum three iterations completed; 16 failed to converge after 10 iterations. Furthermore, 29 clusters had T_X error bars greater than 50 per cent of the central value and are therefore removed. Another three clusters are removed due to extensive variation in the temperature fit as measured by the coefficient of variance. Furthermore, during the initial eyeballing process, 21 of these clusters were highlighted as being potentially affected by chips gaps, low counts, or dominant point sources affecting the XAPA region. Although these clusters ran through the XCS3P process, we are not confident in the temperature or luminosity outputs. Therefore, we remove these clusters entirely from the scaling relation fit; however, they are retained on the scaling plots for reference circled in red (e.g. Fig. 8) and it should be noted that many are not outliers, suggesting we have been overly cautious. Finally, we remove the three clusters that returned a redshift in scanning mode > 10 per cent than the catalogue value (see Section 3.2) but again leave these on the plot highlighted in red. We designate this final sample of 184 clusters as $XCS_{scaling}$.

For the scaling relations involving richness, we exclude a further 10 clusters from the fit, but again retain these on the plot for reference highlighted by black circles. Six of these 10 clusters are because they have a *MASKFRAC* > 0.20 and the other 4 are removed from the fit because the richness measured for the X-ray cluster in scanning mode differs from the matched catalogue entry by > 30 per cent (see Section 3.2). We therefore use 174 clusters from the $XCS_{scaling}$ sample for scaling relations involving richness.

4.2.3 Luminosity upper limits

For the 291 optically detected clusters in RM_{cut} with no matched XCS source, we estimate upper limit luminosities using the same methodology as G22b (see section 3.3 of that paper). Briefly, we estimate an initial r_{500} using a fixed temperature of 3 keV in equation (1). This is chosen to avoid introducing any bias from estimating temperature from the T_X–λ relation, given temperature is correlated to luminosity. We measure a 3σ count rate upper limit using the SAS tool EREGIONANALYSE and convert the count rate upper limit to a flux. This is done using an energy conversion factor again assuming a fixed temperature of 3 keV and the redMaPPer estimated redshift. This flux is then converted to an upper limit. While these upper limits are a simplistic estimate (the initial count rate estimate from EREGIONANALYSE does not assume cluster emission), they qualitatively follow a similar distribution to the analysis presented in Section 3.3 (which presents a more detailed analysis of undetected redMaPPer clusters in our X-ray data).

5 SCALING RELATIONS

Here, we present the measured scaling relation between X-ray luminosity and X-ray temperature (L_X–T_X) and between the X-ray properties and the optical observable, λ (T_X–λ and L_X–λ). We assume self-similarity (Kaiser 1986) and note that the analysis presented herein does not account for selection biases (namely, Eddington and Malmquist), but these will be explored in a future paper when a simulation-based XCS selection function is well established. The scaling relations presented should be considered with this in mind.

5.1 Fitting the data

We fit the data using the LIRA (**LI**near **R**egression in **A**stronomy, see Sereno (2016) for further details on the LIRA) package (in R). Each scaling relation is fitted with a power law of the form

$$Y = A + B \cdot Z \pm \epsilon, \tag{2}$$

where $\text{var}(\epsilon) = \sigma^2_{Y|Z}$ and Z is the intrinsic cluster property. For simplicity, the scaling relations are denoted by the cluster properties in question and the scatter given by σ (for example, see equation (3)).

For the L_X–T_X relation, we fit the data using a power-law relation between $L^{r500}_{X,bol}$ and T_X, expressed as follows:

$$\log\left(\frac{L^{r500}_{X,bol}}{E(z)^{\gamma_{LT}} L_0}\right) = \log(A_{LT}) + B_{LT}\log\left(\frac{T_X}{T_0}\right) \pm \sigma_{L|T}, \tag{3}$$

where A_{LT} denotes the normalization, B_{LT} the slope, and $\sigma_{L|T}$ the intrinsic scatter. γ_{LT} is the evolution with redshift and is set equal to 1 as per the self-similar expectation. Note that the intrinsic scatter is given in natural log space and can be interpreted as the fractional scatter. Normalization values were set to $L_0 = 0.7 \times 10^{44}$ erg s^{-1} and $T_0 = 2.5$ keV, roughly median values of the samples.

For the L_X–λ relation, we fit the data using a power-law relation expressed as follows:

$$\log\left(\frac{L^{r500}_{X,52}}{E(z)^{\gamma_{L\lambda}} L_0}\right) = \log(A_{L\lambda}) + B_{L\lambda}\log\left(\frac{\lambda_{RM}}{\lambda_0}\right) \pm \sigma_{L|\lambda}, \tag{4}$$

where $A_{L\lambda}$ denotes the normalization, $B_{L\lambda}$ represents the slope and $\sigma_{L|\lambda}$ denotes the intrinsic scatter (once again the values are given in natural log space). γ_{LT} is set equal to 2 as per the self-similar expectation. The values of L_0 and λ_0 were set as 0.7×10^{44} erg s^{-1} and 60, respectively.

For the T_X–λ relation, we fit the data using a power-law relation expressed as follows:

$$\log\left(\frac{T^{r500}_X}{T_0}\right) = \log(A_{T\lambda}) + B_{T\lambda}\log\left(\frac{\lambda_{RM}}{\lambda_0}\right) \pm \sigma_{T|\lambda}, \tag{5}$$

where $A_{T\lambda}$ denotes the normalization, $B_{T\lambda}$ represents the slope, and $\sigma_{T|\lambda}$ and denotes the intrinsic scatter (once again the values are given in natural log space). γ_{LT} is set equal to 2/3 as per the self-similar expectation. For a wide range of redshifts, the quantity $E(z)^{-\frac{2}{3}} T$ should be a closer reflection of halo mass, M, than temperature alone (Farahi et al. 2019). The values of T_0 and λ_0 were set as 2.5 keV and 60, respectively.

5.2 Fitted scaling relations

5.2.1 The L_x–T_x relation

The L_X–T_X relation for the $XCS_{scaling}$ sample is shown in Fig. 8 (top), given for $L^{r500}_{X,bol}$. We also consider the changes in the scaling relation
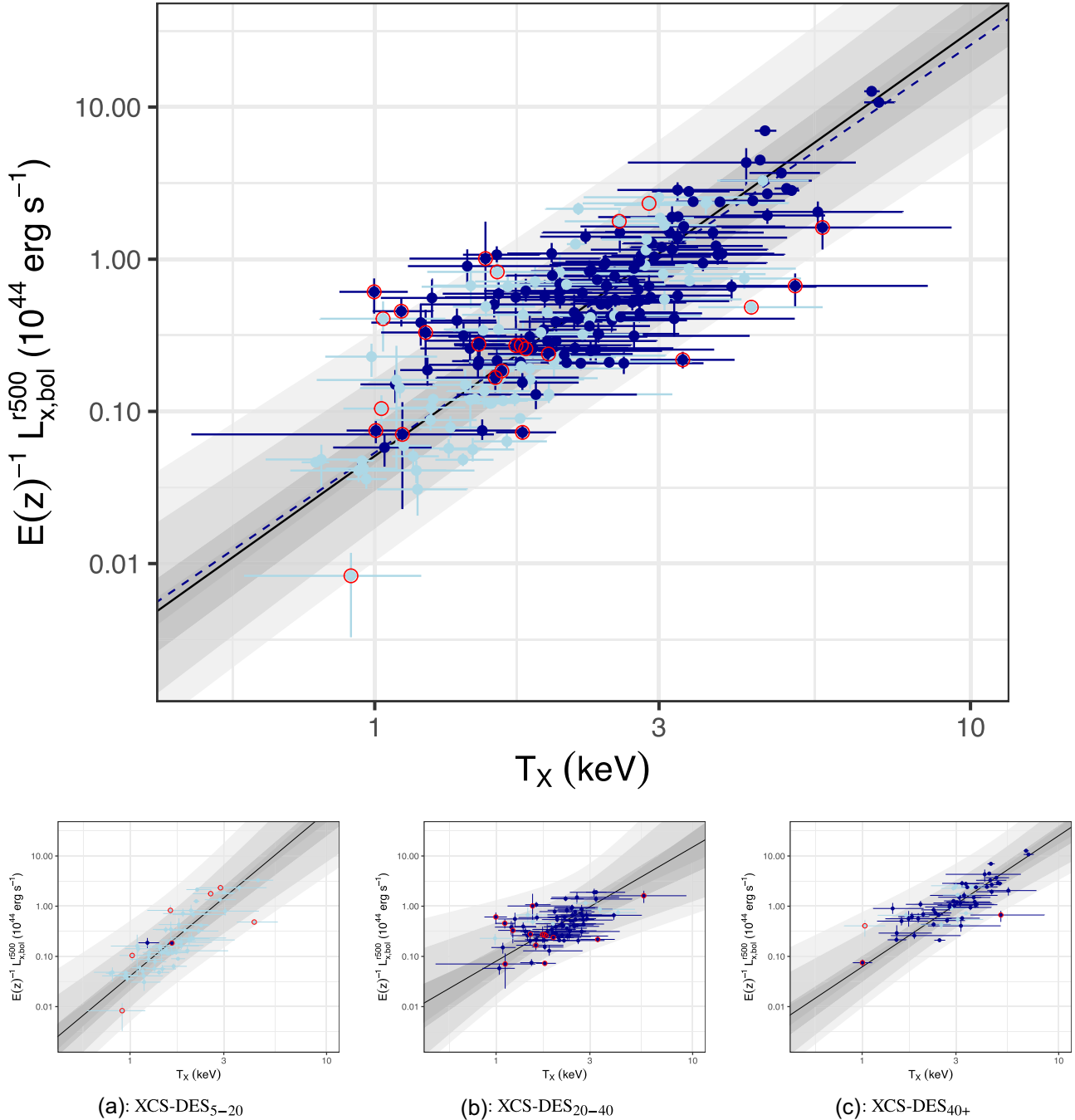
Figure 8. Luminosity–temperature (L_X–T_X) relations in different richness bins. These were derived from the XCS$_{scaling}$ sample (see Section 4.2.2). Dots in dark (light) blue represent clusters from XCS$_{scaling}$ with (without) a match in the optical catalogue (with $\lambda > 20$ and $0.1 < z < 0.9$). The best fit and the corresponding 1, 2, 3σ regions for each relation are shown by the black line and the dark, medium, and light grey regions, respectively. Dots circled in red are included for completeness, but were not included in the L_X–T_X (see Section 4.2.2 for details of the fitting procedure). The dark blue dashed line is the best fit for the RM$_{XCS}$ sample. Top: XCS-DES$_{All}$. Bottom (a) XCS-DES$_{5-20}$. (b) XCS-DES$_{20-40}$. (c) XCS-DES$_{40+}$.

as a function of richness using three different richness bins: $5 < \lambda < 20$, $20 < \lambda < 40$, and $\lambda > 40$ (Fig. 8 bottom left, middle, right, respectively). The best fit for each sample is represented by the solid black line and the grey channels represent 1σ, 2σ, and 3σ residual scatter. The best-fitting line for the optically selected sample (RM$_{scaling}$) is shown by the dashed blue line. Those clusters that are excluded from the fit (see Section 4.2.2) are circled in red. We have tested the fit inclusive of these clusters and, as they are not significant outliers, their

exclusion does not make a significant difference to the fit parameters. Dark blue points are X-ray clusters with a counterpart in the RM$_{cut}$ sample. Light blue points are X-ray clusters without a counterpart in RM$_{cut}$ sample. Best-fitting parameters for each subsample are given in Table 2. To allow easier comparison to other works, Table 2 also includes fitted values for the 0.5–2.0 keV energy band (i.e. $L_{X,52}^{r500}$). The slope of the $L_{X,bol}^{r500}$–T_X relation for XCS$_{scaling}$ is consistent with previous studies (e.g. Pratt et al. 2009; Eckmiller, Hudson & Reiprich

Table 2. Best-fitting parameters for $L_X - T_X$, $L_X - \lambda$, and $T_X - \lambda$ scaling relations given by equations (3), (4), and (5), respectively (see Section 5.1). For each relation, parameters are given for the X-ray-selected ($T_{X,err} < 50$ \$ per cent and $0.1 \leq z \leq 0.9$) cluster sample. γ is set to 1 for all the $L_X - T_X$ relations, 7/3 for the bolometric $L_X - \lambda$ relation, 2 for the $L_{X,52} - \lambda$ relation and 2/3 for the $T_X - \lambda$ relation, all as per self-similar expectations.

Relation (sample)	Normalization	Slope	Residual scatter	Cluster count	Fitted points
$L_{X,\mathrm{bol}}^{r500} - T_X^{r500}$	A_{LbT}	B_{LbT}	σ_{LbT}		
$\mathrm{XCS_{scaling}}$	0.94 ± 0.05	2.79 ± 0.11	0.43 ± 0.02	208	184
$\mathrm{XCS_{scaling\_5-20}}$	1.15 ± 0.22	3.27 ± 0.31	0.49 ± 0.04	62	55
$\mathrm{XCS_{scaling\_20-40}}$	0.92 ± 0.1	2.27 ± 0.5	0.42 ± 0.04	86	72
$\mathrm{XCS_{scaling\_40+}}$	0.97 ± 0.11	2.61 ± 0.26	0.38 ± 0.03	60	57
$\mathrm{RM_{scaling}}$	0.89 ± 0.06	2.59 ± 0.17	0.41 ± 0.02	120	106
$L_{X,52}^{r500} - T_X^{r500}$	A_{LbT}	B_{LbT}	σ_{LbT}		
$\mathrm{XCS_{scaling}}$	0.36 ± 0.02	2.41 ± 0.12	0.46 ± 0.02	208	184
$\mathrm{XCS_{scaling\_5-20}}$	0.44 ± 0.08	2.9 ± 0.31	0.51 ± 0.04	62	55
$\mathrm{XCS_{scaling\_20-40}}$	0.34 ± 0.04	1.71 ± 0.49	0.48 ± 0.03	86	72
$\mathrm{XCS_{scaling\_40+}}$	0.38 ± 0.04	2.16 ± 0.25	0.4 ± 0.03	60	57
$\mathrm{RM_{scaling}}$	0.36 ± 0.02	2.19 ± 0.17	0.44 ± 0.02	120	106
$L_X^{r500} - \lambda_{\mathrm{RM}}$	$A_{L\lambda}$	$B_{L\lambda}$	$\sigma_{L\lambda}$		
X-ray selected	1.31 ± 0.12	1.37 ± 0.1	0.74 ± 0.02	208	174
$L_{X,52}^{r500} - \lambda_{\mathrm{RM}}$	$A_{L52\lambda}$	$B_{L52\lambda}$	$\sigma_{L52\lambda}$		
X-ray selected	0.51 ± 0.04	1.22 ± 0.09	0.67 ± 0.02	208	174
Optically selected (inc UL)	0.57 ± 0.05	1.5 ± 0.14	0.58 ± 0.02	404	383
Optically selected (exc UL)	0.56 ± 0.05	1.49 ± 0.14	0.58 ± 0.02	120	106
$T_X^{r500} - \lambda_{\mathrm{RM}}$	$A_{T\lambda}$	$B_{T\lambda}$	$\sigma_{T\lambda}$		
X-ray selected	1.07 ± 0.04	0.48 ± 0.04	0.26 ± 0.01	208	174
Optically selected	1.13 ± 0.05	0.62 ± 0.07	0.23 ± 0.01	120	106

2011; Lovisari et al. 2020; Bahar et al. 2022; Giles et al. 2022b). However, we find some tentative evidence that the slope of the $L_{X,bol}^{r500} - T_X$ relation is steeper when limiting the sample to lower richness (i.e. lower mass) clusters. See Section 6.1.1 for further discussion. We note that the inclusion of the additional 88 clusters with $\lambda < 20$ in the full X-ray sample ($\mathrm{XCS_{scaling}}$) compared to the optical sample ($\mathrm{RM_{scaling}}$) does not significantly alter the $L_X^{r500} - T_X$ relation.

5.2.2 The $T_x - \lambda$ and $L_x - \lambda$ relations

The X-ray-selected $T_X - \lambda$ relation is shown in Fig. 9 and the $L_{X,52}^{r500} - \lambda$ relation is shown in Fig. 10 (left). For completeness, we also show the $L_{X,52}^{r500} - \lambda$ relation for the optically selected sample with upper limits for non-detections as described in Section 4.2.3. In both Figs 9 and 10, we again highlight clusters that have been excluded from the fit due to uncertain luminosity or temperature measurement (red circled points). Additionally, clusters with an uncertain λ are circled in black and excluded from the fit (see Section 4.2.2). The best-fitting parameters for each relation are given in Table 2.

As found in other studies (e.g. G22b), the residual scatter in the $L_X - \lambda$ relation is more than 3 times that of the $T_X - \lambda$ relation, although this is consistent with the differing slopes. The slopes for both relations are statistically similar to G22b, but the measured scatter of the $L_x - \lambda$ relation in this study is somewhat smaller (0.80 ± 0.02 versus 1.07 ± 0.06 in G22b). It is worth noting that when considering only the serendipitous subsample from G22b, our scatter is remarkably similar for the $L_X - \lambda$ relation (0.80 ± 0.02 versus 0.79 ± 0.08). This should be expected given our sample is selected from survey regions (i.e. they are all serendipitously detected) and shows the possibility of creating larger samples from serendipitous X-ray cluster detections in the full XCS catalogue. We note that this is predicated on the assumption that the serendipitous population should have a selection function that is

easier to model, in comparison to archival targeted samples. Creating larger serendipitous *XMM* samples is of particular importance with upcoming large area surveys (e.g. the Vera C. Rubin Observatory's upcoming LSST) and their overlap with the *XMM* archive (see Section 6.3). As shown in G22b, simply matching clusters detected in an incomplete archive leads to differences between the measured scaling relations between *XMM* targeted and serendipitously detected clusters. If we are able to use serendipitously detected clusters, a wealth of previously unused sources becomes available for study.

Finally, we compare the $T_X - \lambda$ relation found here to that found in Farahi et al. (2019, hereafter F19). F19 used the redMaPPer cluster catalogue constructed from 1 year of DES observations to probe the $T_X - \lambda$ relation. The redMaPPer catalogue in F19 was matched to all available *XMM* data to measure X-ray properties for their clusters. Hence, the sample contained a mix of clusters specifically targeted by *XMM* and those found serendipitously (similar to the analysis of G22b). Due to the unknown selection of targeted clusters in archival data, it is an important point of comparison to our work to investigate any systematic effects introduced by the inclusion of these clusters. We find that the slope and residual scatter of the $\mathrm{RM_{scaling}}$ sample is consistent with that of F19 (see their Table 2 for best-fitting parameters of their *XMM* sample). This consistency is particularly relevant as the $T_X - \lambda$ relation derived in the F19 paper informs the scatter prior on the stacked mass–richness relation assumed in the DESY1 cosmology analysis (Abbott et al. 2020).

6 DISCUSSION

6.1 Scaling relations

6.1.1 Richness dependence

Assuming clusters demonstrate self-similarity, the X-ray temperature and X-ray bolometric luminosity should be related with a power law
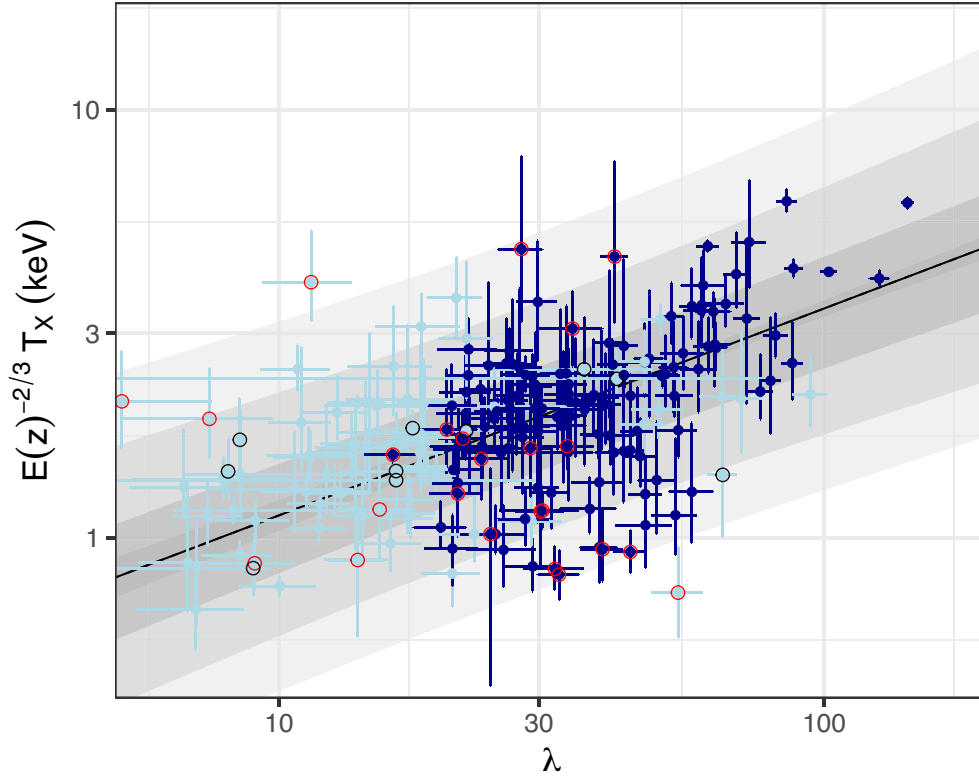
Figure 9. The temperature–richness (T_X–λ) relation of the XCS$_{\rm scaling}$ sample. Points in dark (light) blue represent clusters from the XCS$_{\rm scaling}$ sample with (without) a match in the optical catalogue (with $\lambda > 20$ and $0.1 < z < 0.9$). The best-fitting line is given by the black solid line and the corresponding 1, 2, 3σ residual scatters are shown by the dark, medium, and light grey regions, respectively. Points highlighted in red (indicating an unreliable X-ray value) and black (indicating an unreliable richness value) are excluded from the fit (see Section 4.2.2 for details of the fitting procedure).
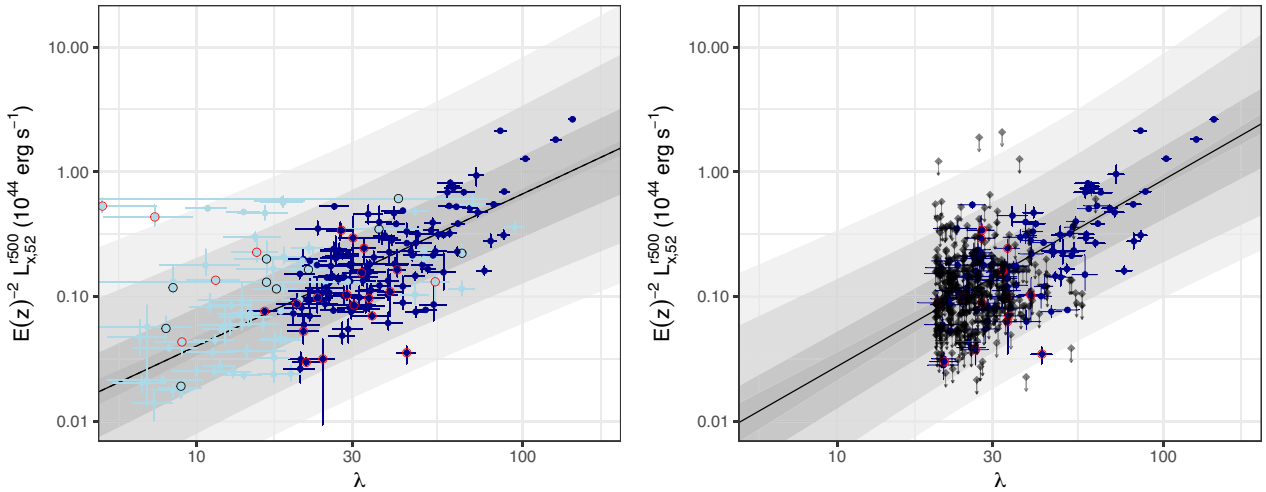
Figure 10. Luminosity–richness ((Left): $L_{X,52}^{r500} - \lambda$) relation for the XCS$_{\rm scaling}$ sample. (Right): $L_{X,52}^{r500} - \lambda$ relation for the RM$_{\rm scaling}$ sample, including 291 upper limit luminosities (see Section 4.2.3 for details) for undetected clusters (given by the black points with downward arrows for the $L_{X,52}^{r500}$ limit). See Fig. 9 for further caption details.

of slope 2. In this work, the observed slope between luminosity and temperature is somewhat steeper, which is consistent with other studies. See Lovisari et al. (2021, Table 2) for a selection of scaling relation properties from the literature. This is likely due to the oversimplified assumption that gravity is the sole heating mechanism within the clusters' physics, as well as the gas fraction increasing as a function of mass (e.g. Eckert et al. 2016).

The literature is more divided when it comes to comparing the slope of the L_X–T_X relation between clusters and groups; for a more detailed discussion, see Lovisari et al. (2021). Previous work has shown that scaling relations can be modelled by a broken power law, highlighting a transition between the cluster and group scale (e.g. Kettula et al. 2015; Lovisari, Reiprich & Schellenberger 2015). However, it is noted that other works (e.g. Sun et al. 2009; Zou
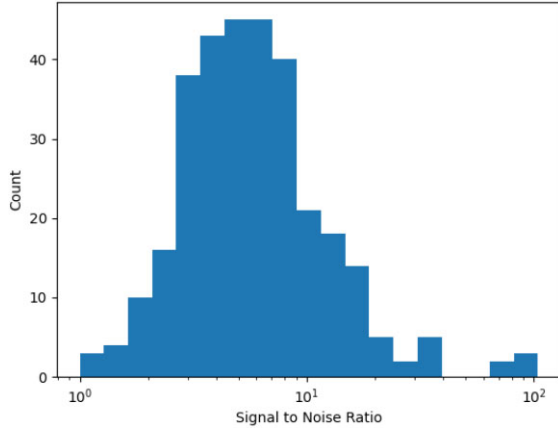
Figure 11. Signal-to-noise distribution for the XCS$_{optically\_confirmed}$ data set. SNR is taken from the initial XAPA region for the PN camera.

et al. 2016) do not observe any inconsistencies between the slopes of low- and high-mass scaling relations. Results from simulations, however, do indicate the presence of a break, or gradual change, in the slope when modelling scaling relations (e.g. Le Brun et al. 2014; Farahi et al. 2018). Recently, Pop et al. (2022) used 30 000 mock haloes from the TNG300 simulations covering the $M_{500,c} = (10^{12} - 2 \times 10^{15})$ M$_\odot$ mass range, to study various scaling relations. Pop et al. (2022) found strong evidence for a break in the modelled relations, occurring between $M_{500,c} \sim 3 \times 10^{13} - 2 \times 10^{14}$, depending on the scaling relation considered.

To investigate a possible break in the slope of $L_X–T_X$ relation considered in the work, we have divided the full X-ray sample into bins of $\lambda < 20$, $20 < \lambda < 40$, and $\lambda > 40$ as an illustration. Using the mass–richness relation of McClintock et al. (2018), these bins correspond to $M_{200,m} \lesssim 1.2 \times 10^{14}$ M$_\odot$, $1.2 \lesssim M_{200,m} \lesssim 3.0 \times 10^{14}$ M$_\odot$, and $M_{200,m} \gtrsim 3 \times 10^{14}$ M$_\odot$. The slope and normalization of the $L_{X,bol}^{r500}–T_X$ relation for the $20 < \lambda < 40$ and $\lambda > 40$ bins are statistically similar to the total sample, but it is noted that the lower richness (and by definition, lower mass) bin relation is marginally steeper with a higher normalization. The steeper slope at these lower richnesses may support the broken power-law model of scaling relations; however, the slope of the $\lambda < 20$ clusters is only steeper than the $\lambda > 40$ clusters at the $\sim$1.6σ level. One plausible reason for the steepening of the relation at low richnesses is the increased fraction of AGN within clusters as a function of decreasing mass (e.g. Noordeh et al. 2020). It is possible that a higher fraction of the low λ bin has increased AGN contamination, leading to an increased luminosity and hence steepening the slope of the $L_X–T_X$ relation.

6.1.2 Effect of low signal-to-noise clusters on scaling relations

As per Section 4.2.2, the only cut we make on the data is removing clusters where the temperature error bar is greater than 50 per cent of the central value i.e. post-processing. However, we are aware that due to the serendipitous nature of the X-ray detections, the X-ray sample includes low signal-to-noise observations, as shown in Fig. 11. We have tested the effect of these low SNR clusters on our derived scaling relations by fitting the data (following the same fitting method as in Section 5.1), but excluding all clusters with an SNR < 5. The SNR ratio used here was estimated from the PN spectra used in the XSPEC fits (as generated in Section 4.1) and represents an SNR within our estimate of r_{500} for the cluster. Excluding these low SNR clusters

makes no statistical difference to the derived scaling relations, and so we use all data points, regardless of their SNR.

6.2 Comparison to previous studies

One of the most analogous comparisons to the work presented here is that of Ota et al. (2023, hereafter O22), who constructed a photometrically selected sample of clusters from Hyper Suprime-Cam (HSC) analysed using the CAMIRA red-sequence cluster finder Oguri (2014). The clusters were selected over 140 deg^2 that coincided with the eROSITA Final Equatorial-Depth Survey (eFEDS Brunner et al. 2022), and hence have complete X-ray coverage. O22 cross-matched 41 clusters with a richness $\hat{N}_{mem} > 40$ with the eFEDS cluster catalogue (Liu et al. 2022), finding 32 CAMIRA clusters with a match to the eFEDS catalogue, in order to probe various scaling relations. Using these 32 clusters, O22 find a slope of the $L_X–T_X$ relation of 1.87 ± 0.45. Note, this result does not account for selection effects. However, O22 do model effects of selection resulting in a steeper slope (2.08 ± 0.46), but we compare to the uncorrected slope for consistency with the work presented here. To provide a more robust comparison to O22, we limit the RM$_{scaling}$ scaling sample to clusters with $\lambda > 40$ and re-fit for the $L_X–T_X$ relation (following the method as in Section 5.1). Using only $\lambda > 40$ RM$_{scaling}$ clusters, we find a slope of the $L_X–T_X$ relation of 2.61 ± 0.27. While steeper than the O22 relation, the difference is only significant at the 1.5σ level.

Another point of comparison is the work of Giles et al. (2022a, hereafter G22a), who presented a comparison of optically and X-ray-selected clusters over $\approx$16 deg^2 of the XXL-N region. While the G22a optical clusters were spectroscopically selected from the Galaxy and Mass Assembly survey (GAMA, Driver et al. 2011) group catalogue (version G3Cv10, constructed from the group detection routine of Robotham et al. 2011), and hence different from the photometric selection used here, the comparison is still warranted. Note the X-ray data in G22a were selected from the XXL-N survey (Pierre et al. 2016), as used in this work. The main result presented in G22a was an apparent increase in the scatter of the luminosity–velocity dispersion ($L–\sigma_v$) for their X-ray-selected sample compared to the optically selected sample.

While we cannot compare a $L–\sigma_v$ relation to the one done in G22a, the most appropriate comparison we can make is the $L_X–\lambda$ relation between the optically and X-ray selected samples. We find that the scatter of the XCS$_{scaling}$ $L_X–\lambda$ relation is only 10 per cent higher than that of the RM$_{scaling}$ sample. This is significantly less than the factor 2.7 times higher scatter of the G22a X-ray-selected sample compared to their optically selected sample. It is noted in G22a that due to the small sample size, a small number of high luminosity outliers in the X-ray-selected sample were affecting the measurement of the scatter. Since our sample is significantly larger than that in G22a, we are less affected by small population outliers (but note that a larger fraction of outliers would still indeed affect our results). As mentioned in Section 5.2, removal of low SNR clusters does not significantly impact the measured relation. We not only note that for all the relations studied in this work, the XCS$_{scaling}$ sample presents a marginally larger scatter than the RM$_{scaling}$ sample, but also note that none of the differences in scatters are significantly different.

Our results are more in line with that of Connelly et al. (2012, hereafter C12). C12 utilized two regions of the Canadian Network for Observational Cosmology Field Galaxy Redshift Survey 2 (CNOC2) with overlapping contiguous *Chandra* observations to construct optically and X-ray selected samples. Broadly, they found that the
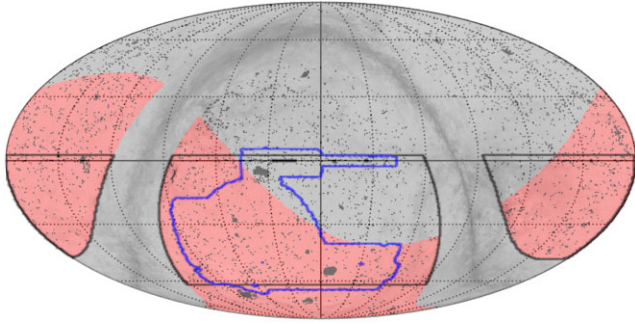
Figure 12. Full sky map highlighting the location and size of *XMM* observations given by the dark grey points. In pink, the eRASS*DE* region (excluding the Galactic plane) is highlighted. The DES and LSST survey footprints are given by the blue and black outlines, respectively. The light-grey background map displays the polarized dust emission map from *Planck*.

scatter of the L_X–σ_v relation were consistent for both sample of clusters, as found in the work presented here.

6.3 Predicted X-ray cluster detections in the era of the Rubin Observatory

Given the samples constructed in this work, we can estimate the number of potential clusters in common between those detected by the upcoming LSST, planned to be carried out by the Rubin Observatory, and the *XMM* archive. The LSST Wide Fast Deep (LSST-WFD) survey (The LSST Dark Energy Science Collaboration et al. 2018) will aim to cover $\approx 14\,000$ deg^2 of the southern sky (excluding the Galactic plane). Currently, the *XMM* archive covers 504 deg^2 of the proposed footprint of the LSST-WFD (including the 57.4 deg^2 of observations used in this work). This is shown in Fig. 12, with the sky plot highlighting the position of all currently available *XMM* observations (grey points). The proposed area of the LSST-WFD is given by the black outline. Given the incompleteness of the X-ray detections of RM clusters in this work (see Section 3), the limiting factor will be the depth of the *XMM* observations. Therefore, using the current DESY3 sample as a precursor should provide a representative indication of the number of LSST-WFD clusters detected in the *XMM* archive. Given the 178 cluster in the RM$_{XCS}$ sample, this leads to a cluster density of 3.1 clusters per deg^2. For the full overlap of the LSST-WFD with the *XMM* archive, we predict a sample of ≈ 1500 LSST-selected clusters will be detected by *XMM*. Note, however, that ~ 50 per cent of observations in *XMM* archive have a nominal exposure time longer than that of a typical observation used in this work, and hence the predicted number of clusters is likely a lower limit. Furthermore, these estimates are for redMaPPer[5] with $\lambda > 20$ and within $0.1 < z < 0.9$.

Focusing on forecasts for X-ray-selected samples, the XCS$_{opt}$ sample contains 341 clusters, 298 of which have properties (i.e. redshift and richness) returned by redMaPPer. Using these 298 clusters, we determine a source density of ≈ 5.2 clusters per deg^2. Again expanding to the full LSST-WFD with available *XMM* data, we estimate there will be ≈ 2600 X-ray selected clusters. Due to the deeper depth of the LSST compared to DES, this is likely to be a lower limit (e.g. LSST will detect the high redshift X-ray clusters not found by RM using the current DES data, see Section 3). Further

---

[5]Note that redMaPPer is one of a number of cluster finders being tested for use with the LSST

X-ray data will come from the *eROSITA all sky survey* (eRASS). Currently, only the western half (in Galactic coordinates) is due to be publicly released (by the German eROSITA Consortium, we denote this half of the sky eRASS*DE*). The sky region covered by eRASS is given by the pink-shaded region in Fig. 12. To estimate the number of clusters detectable by eFEDS over the LSST-WFD region, we make use of the recently released cluster catalogue from the 140 deg^2 eFEDS (Liu et al. 2022). This sample contains 542 clusters, of which 477 are subsequently optically confirmed (Klein et al. 2022), using the multicomponent matched filter (MCMF) cluster confirmation tool (Klein et al. 2018). Using the optically confirmed sample leads to an eRASS source density of ≈ 3.4 clusters deg^{-2}. We estimate the overlap between the LSST-WFD and eRASS*DE* to be 10 174 deg^2, leading to a potential $\approx 34\,600$ clusters when the final depth eRASS*DE* is released.

7 SUMMARY

In this paper, we consider two samples of clusters, one selected via optical data from the DES and a second using X-ray observations from *XMM-Newton*. The samples are constructed from four survey regions observed by *XMM*, analysed by the XCS that overlap with the DES footprint. We cross-match between the two samples to determine the level of overlap explaining why some optically detected clusters are not being detected in the X-ray observations. We also explore various scaling relations, including the X-ray L_X–T_X relation and the mass observable relations L_X–λ and T_X–λ. We find the following:

(i) Across 57.4 deg^2 of the four survey regions used in this work, there are 468 redMaPPer-detected DES clusters within the parameter space $\lambda > 20$ and $0.1 < z < 0.9$, of which 178 have a visually confirmed X-ray counterpart. By comparison, there are 341 X-ray extended sources detected by XCS, with a visually identified optical red galaxy overabundance coincident with the X-ray source.

(ii) From the samples derived, we find that the redMaPPer sample is $\simeq 38$ per cent matched in terms of X-ray detections. However, as a function of λ, X-ray completeness is ≈ 95 per cent above $\lambda > 60$ and entirely complete above $\lambda > 70$, although the number of clusters in these subsamples is small.

(iii) Based upon the constructed X-ray sample, the redMaPPer catalogue is fully matched to the XCS catalogue for $\lambda > 20$ and $0.1 < z < 0.9$, i.e. all X-ray clusters within this range are recovered in the optical cluster catalogue.

(iv) We found that 46 per cent of redMaPPer clusters undetected by our X-ray data can be explained by the insufficient exposure times of our current observations (based on estimating the X-ray luminosity from their richness and our measured L_X–λ relation). For the other 54 per cent, we found that the X-ray exposure times of current observations become insufficient if we reduce the clusters' luminosities within the measured scatter of the L_X–λ relation.

(v) The L_X–T_X scaling relation for the overall X-ray and optical samples are consistent with each other, and also with serendipitous X-ray cluster samples in the literature.

(vi) Creating subsamples based upon λ cuts, we find that the slope of the L_X–T_X relation is somewhat steeper for lower richness clusters with $\lambda < 20$ compared to $\lambda > 40$, although only significant to the 1.6σ level.

(vii) We have shown that the L_X–λ relation slope and residual scatter is consistent with that for the relation derived from serendipitously detected clusters found in Giles et al. (2022b).

(viii) Additionally, the T_X–λ slope and residual scatter is consistent with the results of Farahi et al. (2019).

(ix) We have shown that the inclusion of low SNR X-ray clusters does not affect the scaling relation fit. However, the binning technique used for low SNR clusters may have an effect on the extraction of X-ray properties from XSPEC. Further work will be undertaken on higher quality X-ray data, and degraded down to lower signal-to-noise, to determine how the binning affects the measurement of cluster properties.

(x) We find that the scatter in each of the scaling relations considered is consistent between the optically and X-ray-selected cluster samples. This is in tension with the previous results of Giles et al. (2022a), using clusters from a smaller area than the surveys used in this work, albeit with different optical selection methods.

(xi) Finally, we estimate that there will be $\approx$1500 *XMM*-detected clusters from those detected by the upcoming LSST and its overlap with the *XMM* archive.

ACKNOWLEDGEMENTS

DATA AVAILABILITY

The X-ray sample used for the catalogue cross-match can be found at: https://users.sussex.ac.uk/~xcs-data/XCS_tests_on_DESY3/xray_sample.csv

The optical sample used for the catalogue cross-match can be found at: https://users.sussex.ac.uk/~xcs-data/XCS_tests_on_DESY3/optical_sample.csv

The data used for the X-ray scaling relations can be found at: https://users.sussex.ac.uk/~xcs-data/XCS_tests_on_DESY3/xray_sample_scaling_data.csv

The data used for the optical scaling relations can be found at: https://users.sussex.ac.uk/~xcs-data/XCS_tests_on_DESY3/optical_sample_scaling_data.csv

REFERENCES

Abbott T. M. C. et al., 2018, Phys. Rev. D, 98, 043526
Abbott T. M. C. et al., 2020, Phys. Rev. D, 102, 023509 (A20)
Anbajagane D., Evrard A. E., Farahi A., Barnes D. J., Dolag K., McCarthy I. G., Nelson D., Pillepich A., 2020, MNRAS, 495, 686
Andreon S., Serra A. L., Moretti A., Trinchieri G., 2016, A&A, 585, A147
Applegate D. E. et al., 2014, MNRAS, 439, 48
Arnaud K. A., 1996, in Jacoby G. H., Barnes J.eds, ASP Conf. Ser. Vol. 101, XSPEC: The First Ten Years. Astron. Soc. Pac., San Francisco, p. 17
Arnaud M., Pointecouteau E., Pratt G. W., 2005, A&A, 441, 893
Arviset C., Guainazzi M., Hernandez J., Dowson J., Osuna P., Venet A., 2002, preprint (arXiv:astro-ph/0206412)
Bahar Y. E. et al., 2022, A&A, 661, A7
Bocquet S. et al., 2019, ApJ,, 878, 55
Brunner H. et al., 2022, A&A, 661, A1
Carvalho G. C., Bernui A., Benetti M., Carvalho J. C., Alcaniz J. S., 2016, Phys. Rev. D, 93, 023530
Connelly J. L. et al., 2012, ApJ, 756, 139 (C12)
Dark Energy Survey Collaboration, 2016, MNRAS, 460, 1270
Driver S. P. et al., 2011, MNRAS, 413, 971
Eckert D. et al., 2016, A&A, 592, A12
Eckmiller H. J., Hudson D. S., Reiprich T. H., 2011, A&A, 535, A105
Farahi A., Evrard A. E., McCarthy I., Barnes D. J., Kay S. T., 2018, MNRAS, 478, 2618
Farahi A. et al., 2019, MNRAS, 490, 3341 (F19)
Flaugher B. et al., 2015, AJ, 150, 150
Freeman P. E., Kashyap V., Rosner R., Lamb D. Q., 2002, ApJS, 138, 185
Giles P. A. et al., 2022a, MNRAS, 511, 1227 (G22a)
Giles P. A. et al., 2022b, MNRAS, 516, 3878 (G22b)
Grandis S. et al., 2021, MNRAS, 504, 1253
HI4PI Collaboration, 2016, A&A, 594, A116

Hou Z. et al., 2014, ApJ, 782, 74

Kaiser N., 1986, MNRAS, 222, 323

Kettula K. et al., 2015, MNRAS, 451, 1460

Klein M. et al., 2018, MNRAS, 474, 3324

Klein M. et al., 2022, A&A, 661, A4

Kravtsov A. V., Borgani S., 2012, ARA&A, 50, 353

Le Brun A. M. C., McCarthy I. G., Schaye J., Ponman T. J., 2014, MNRAS, 441, 1270

Le Brun A. M. C., McCarthy I. G., Schaye J., Ponman T. J., 2017, MNRAS, 466, 4442

Liu A. et al., 2022, A&A, 661, A2

Lloyd-Davies E. J. et al., 2011, MNRAS, 418, 14 (LD11)

Lovisari L., Reiprich T. H., Schellenberger G., 2015, A&A, 573, A118

Lovisari L. et al., 2020, ApJ, 892, 102

Lovisari L., Ettori S., Gaspari M., Giles P. A., 2021, Universe, 7, 139

Mauduit J.-C. et al., 2012, Publ. Astron. Soc. Pac., 124, 714

McClintock T. et al., 2018, MNRAS, 482, 1352

Noordeh E. et al., 2020, MNRAS, 498, 4095

Oguri M., 2014, MNRAS, 444, 147

Ota N. et al., 2023, A&A , 669, A110

Pierre M. et al., 2016, A&A, 592, A1

Planck Collaboration XXIV, 2016, A&A, 594, A24

Pop A.-R. et al., 2022, preprint (arXiv:2205.11528)

Pratt G. W., Croston J. H., Arnaud M., Böhringer H., 2009, A&A, 498, 361

Predehl P. et al., 2021, A&A,, 647, A1

Robotham A. S. G. et al., 2011, MNRAS, 416, 2640

Romer A. K., Viana P. T. P., Liddle A. R., Mann R. G., 2001, ApJ, 547, 594

Rykoff E. S. et al., 2014, ApJ, 785, 104

Rykoff E. S. et al., 2016, ApJS, 224, 1

Sereno M., 2016, Astrophysics Source Code Library, record ascl:1602.006

Sevilla-Noarbe I. et al., 2021, ApJS, 254, 24

Smith R. K., Brickhouse N. S., Liedahl D. A., Raymond J. C., 2001, ApJ, 556, L91

Sun M., Voit G. M., Donahue M., Jones C., Forman W., Vikhlinin A., 2009, ApJ, 693, 1142

The LSST Dark Energy Science Collaboration, 2018, preprint (arXiv:1809.01669)

Vikhlinin A. et al., 2009, ApJ, 692, 1060

Wilms J., Allen A., McCray R., 2000, ApJ, 542, 914

Wu H.-Y. et al., 2022, MNRAS, 515, 4471

Zhang Y. et al., 2019, MNRAS, 487, 2578

Zou S., Maughan B. J., Giles P. A., Vikhlinin A., Pacaud F., Burenin R., Hornstrup A., 2016, MNRAS, 463, 820

APPENDIX A: IMAGE EXAMPLES

Here we present some examples of various images referenced in the main paper. Fig. A1 shows typical images used to eyeball DES images for associated X-ray counterparts. Fig. A2 shows images used to eyeball X-ray images for optical red-galaxy overabundances. Fig. A3 is an example of a DES mask affecting detection of an optical cluster. Fig. A4 shows the 14 high redshift clusters outside the detection limits of redMapper (and thus not in the redMaPPer catalogue) but detected in X-ray. Fig. A5 shows the four X-ray detected clusters that are within the redMaPPer parameter space but are not found in the catalogue.

We note that visual inspection can be prone to human variation. We mitigate this by doing classification sessions in pairs involving discussion. When agreement is not found, a third expert is consulted.

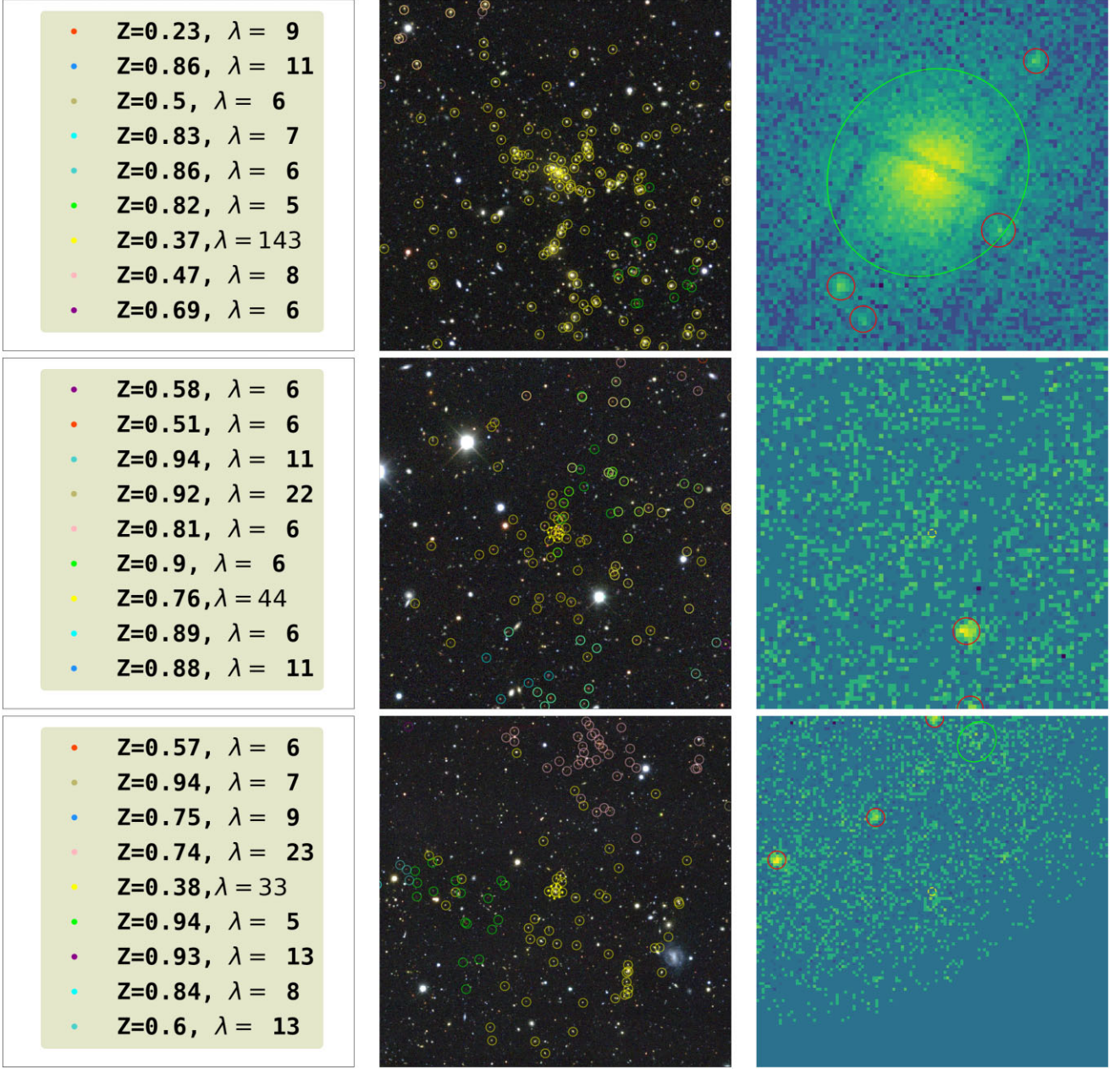**Eyeballing redMaPPer clusters for X-ray counterparts**

•	Z=0.23, λ = 9
•	Z=0.86, λ = 11
•	Z=0.5, λ = 6
•	Z=0.83, λ = 7
•	Z=0.86, λ = 6
•	Z=0.82, λ = 5
•	Z=0.37, λ = 143
•	Z=0.47, λ = 8
•	Z=0.69, λ = 6

•	Z=0.58, λ = 6
•	Z=0.51, λ = 6
•	Z=0.94, λ = 11
•	Z=0.92, λ = 22
•	Z=0.81, λ = 6
•	Z=0.9, λ = 6
•	Z=0.76, λ = 44
•	Z=0.89, λ = 6
•	Z=0.88, λ = 11

•	Z=0.57, λ = 6
•	Z=0.94, λ = 7
•	Z=0.75, λ = 9
•	Z=0.74, λ = 23
•	Z=0.38, λ = 33
•	Z=0.94, λ = 5
•	Z=0.93, λ = 13
•	Z=0.84, λ = 8
•	Z=0.6, λ = 13

Figure A1. Three examples of associating DES optical clusters with XCS X-ray clusters. All images are 6 × 6 arcmins. Left: Legend showing redshift and richnesses for DES clusters in image colour coded by members. Middle: DES image with members of potential clusters coloured together. Right: XCS-processed image showing extended and/or point like X-ray sources. Top row: The XMM image shows an extended associated X-ray source (green ellipse) overlaying the optical cluster. Four point sources (red circles) are also shown. Middle row: The XMM image shows a point-like source (red circle) but no extended emission detected in the region. Bottom row: An extended source is detected in the XMM image, but it is associated with the $z = 0.74$, $\lambda = 23$ DES cluster and not the central DES cluster at $z = 0.38$, $\lambda = 33$. The lack of detection of the central cluster is likely due to the reduced efficiency of the detector towards the edge of the chip.

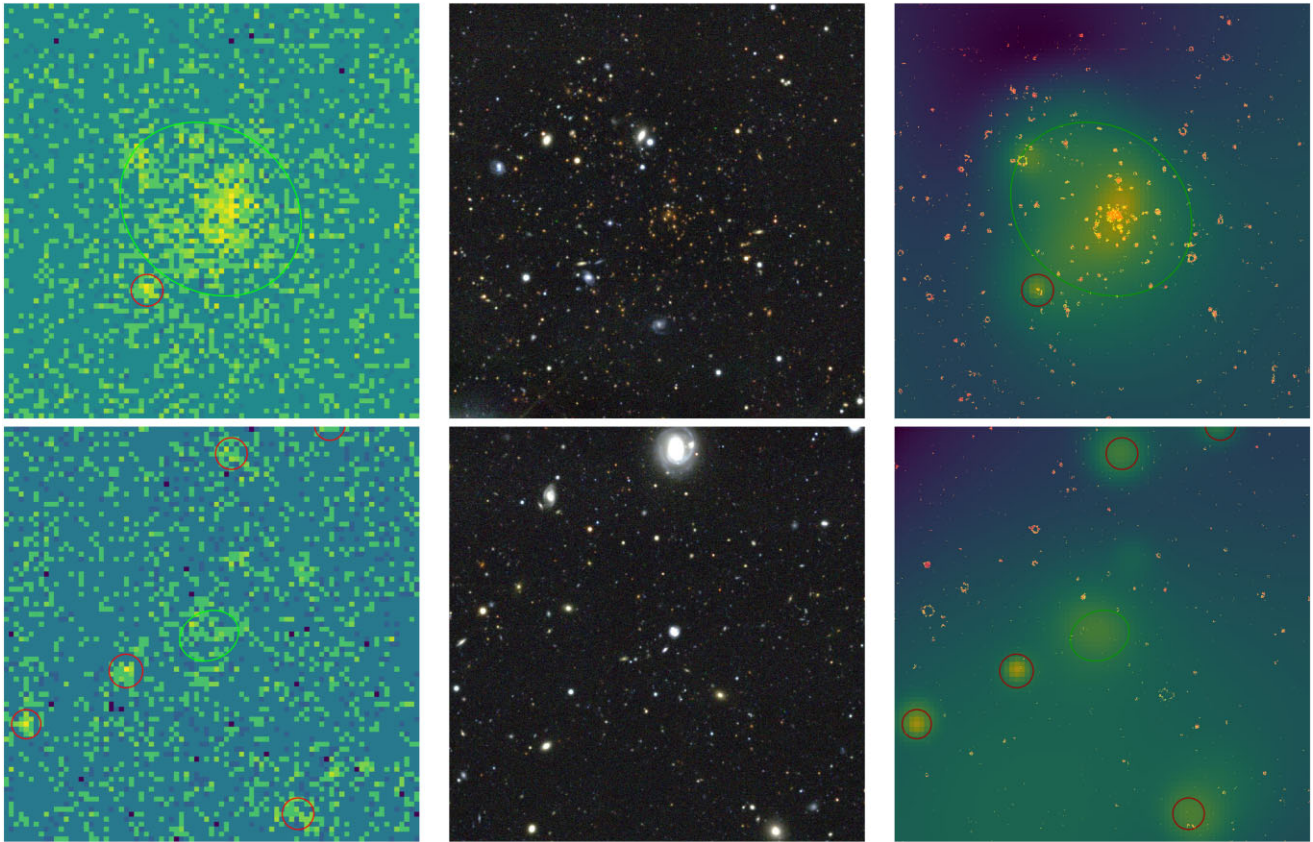**Eyeballing X-ray clusters for redMaPPer counterparts**

Figure A2. Two examples of using contrast-enhanced DES images to confirm X-ray extended sources. All images are 6 × 6 arcmins. Left: XMM image showing XAPA extended source detection. Middle: DES image. Right: XCS image showing smoothed X-ray signal and DES image-enhanced red-channel to highlight red clusters.
Top row: Clear example of red galaxy overabundance in both the pure DES image and the overlay. This extended source is therefore optically confirmed.
Bottom row: Example of a XAPA detection with no red galaxy over abundance showing in the DES image. The contrast enhancements also show no red galaxies. This extended source is thus not optically confirmed.
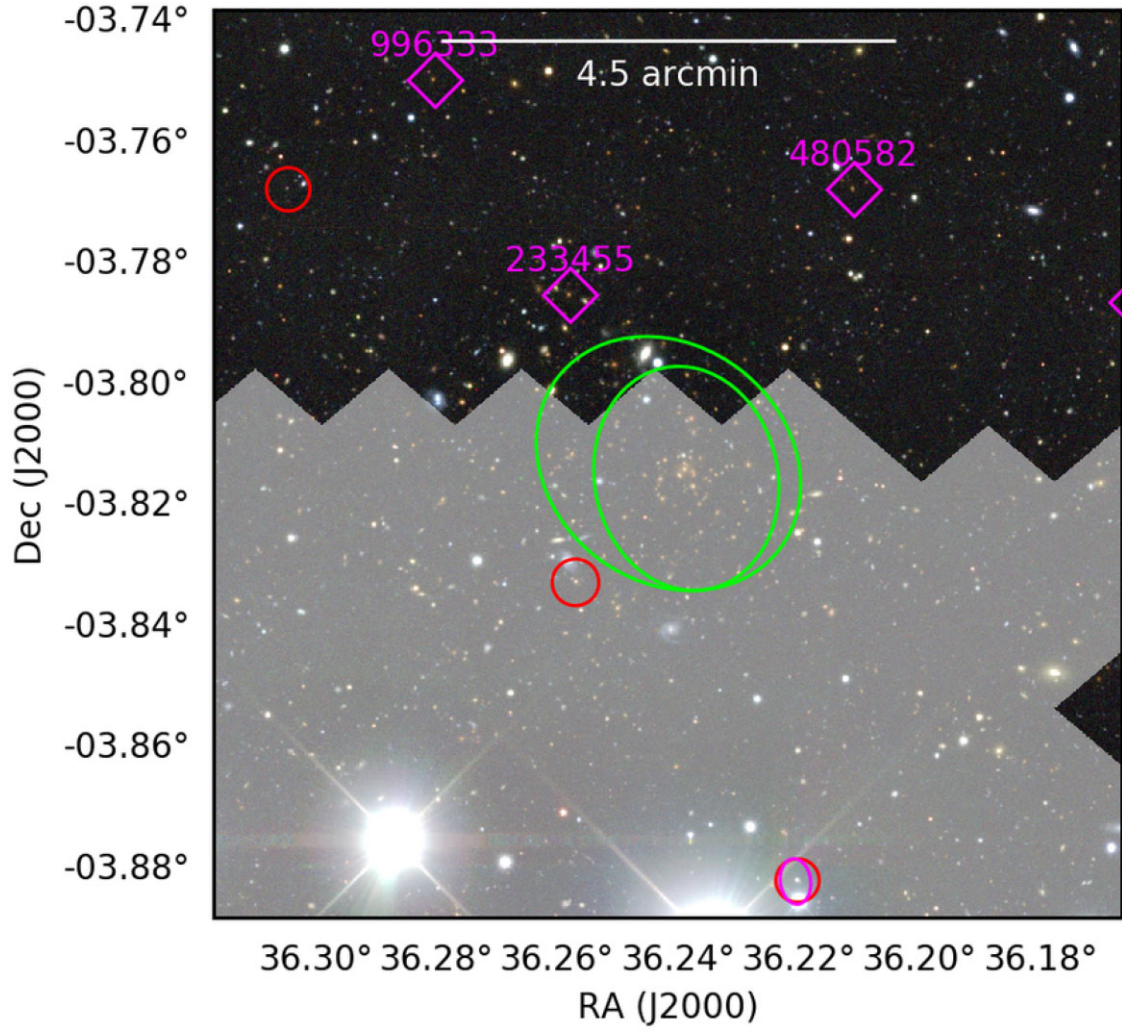
Figure A3. An example of a DES masked region that covers an obvious cluster. This is the same cluster as Fig. A2 top. Again, green ellipses represent X-ray cluster detections whilst purple diamonds represent redMaPPer cluster centroids and their MEM_MATCH_ID. The grey overlay represents the DES Mask caused by the two bright stars at the bottom of the cut-out. As can be seen, the cluster is covered by a mask and, therefore, does not appear in the redMaPPer catalogue despite being clear and obvious.
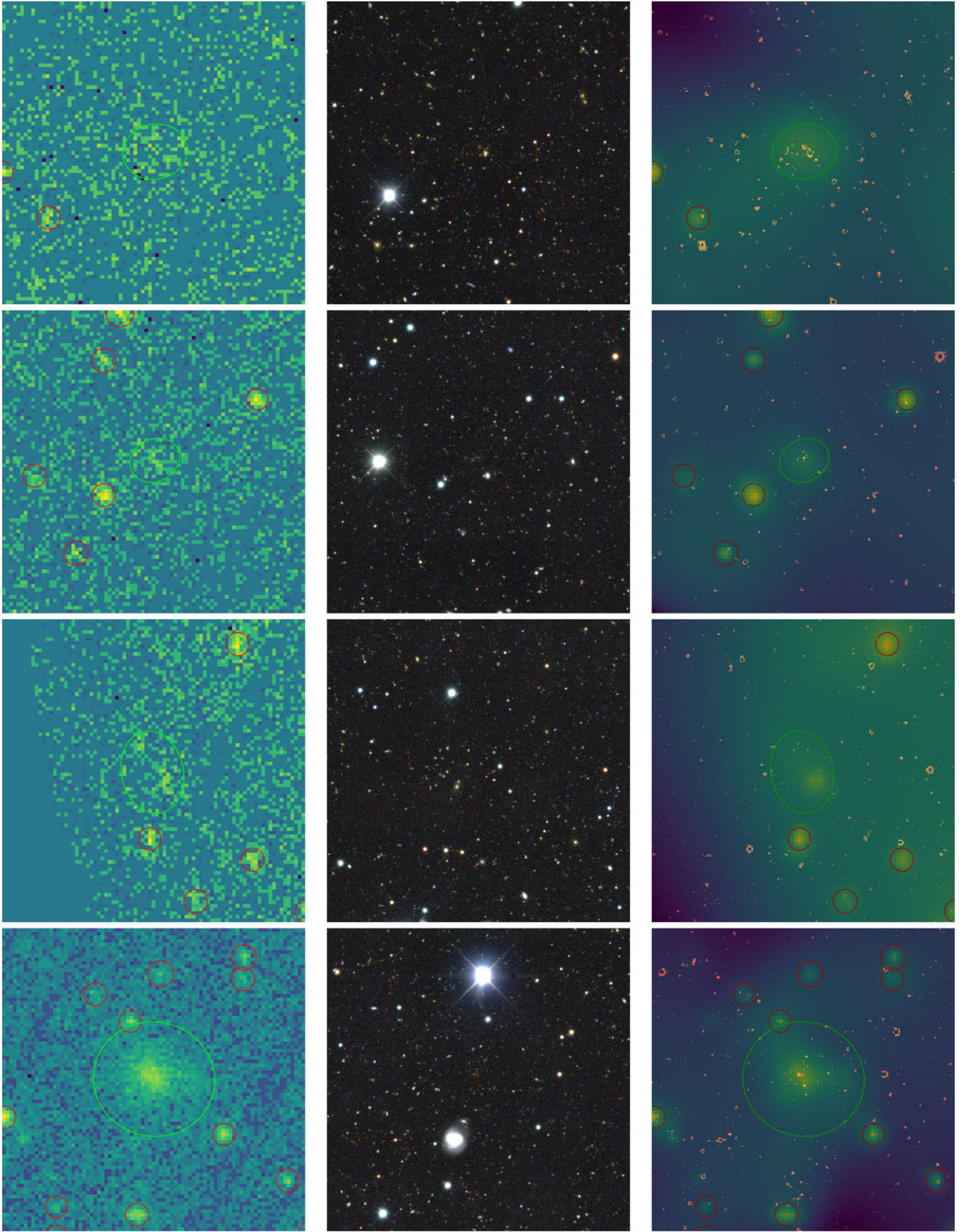
Figure A4. Thirteen examples of using contrast enhanced DES images to show red galaxy overabundances for high redshift X-ray extended sources that are not present in the redMaPPer catalogue. All images are 6×6 arcmins. Left: XMM image showing XAPA extended source detection. Middle: DES image. Right: XCS image showing smoothed X-ray signal and DES image-enhanced red-channel to highlight red clusters.
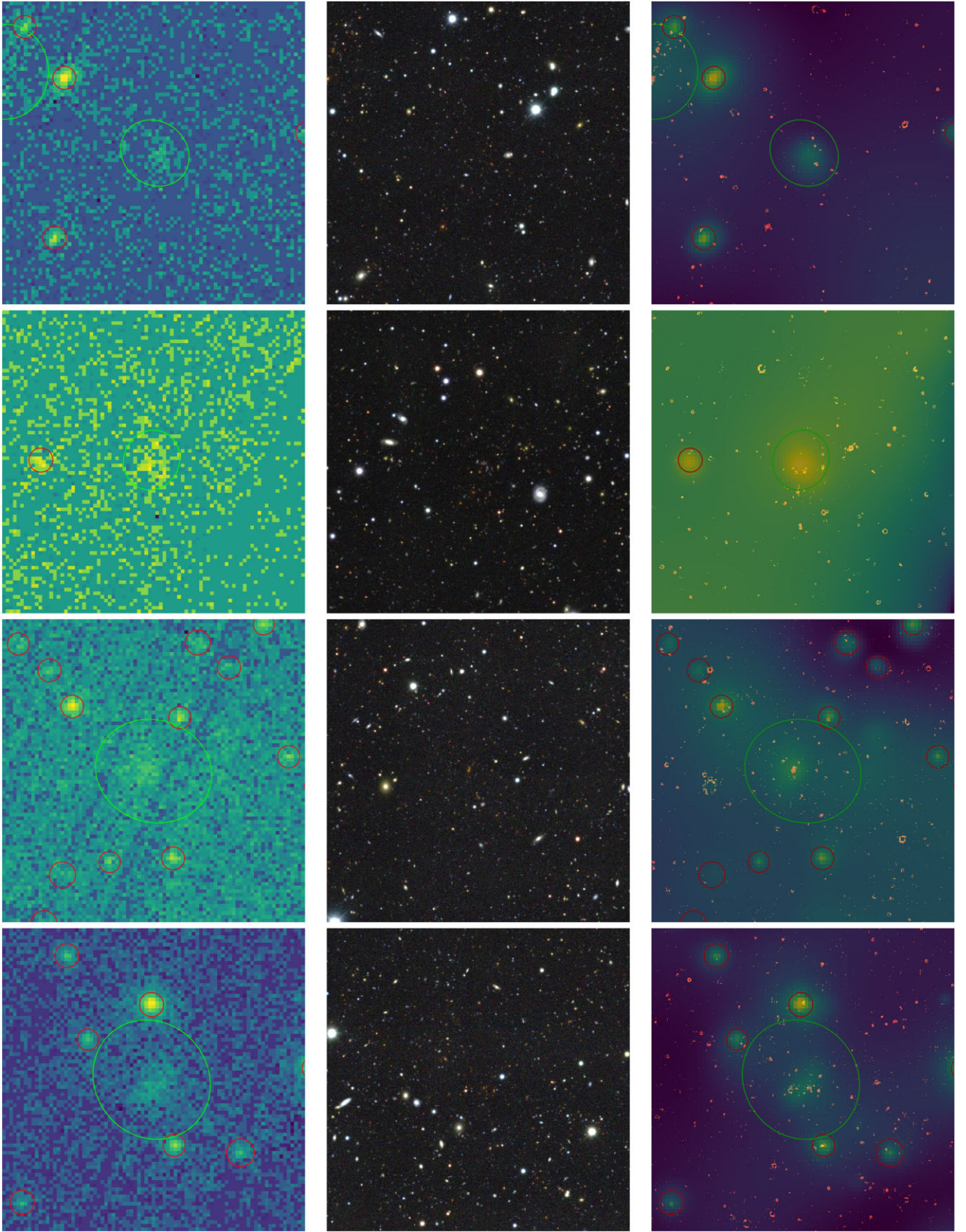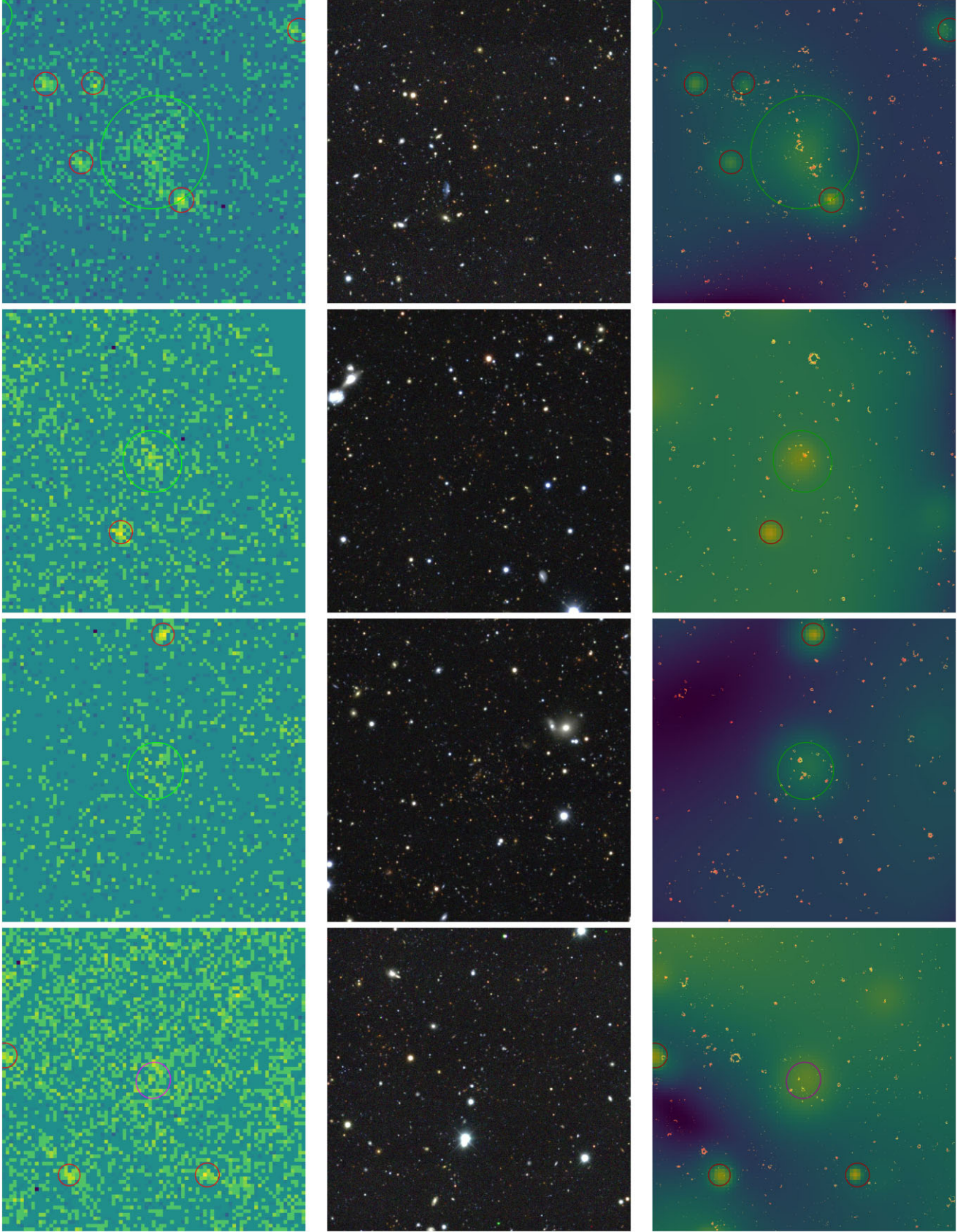
Figure A4 *– continued*
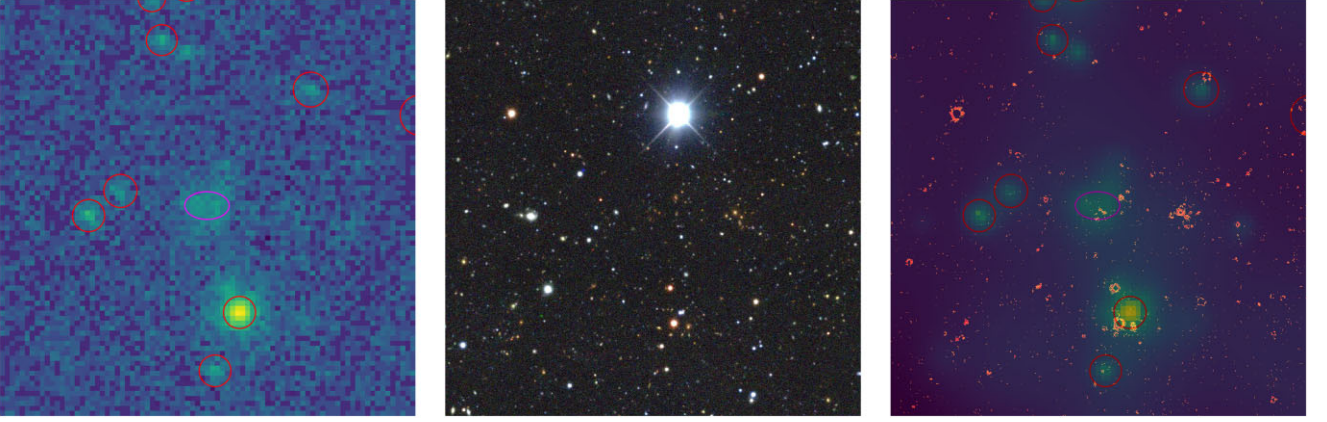
Figure A4 *– continued*

Figure A4 *– continued*

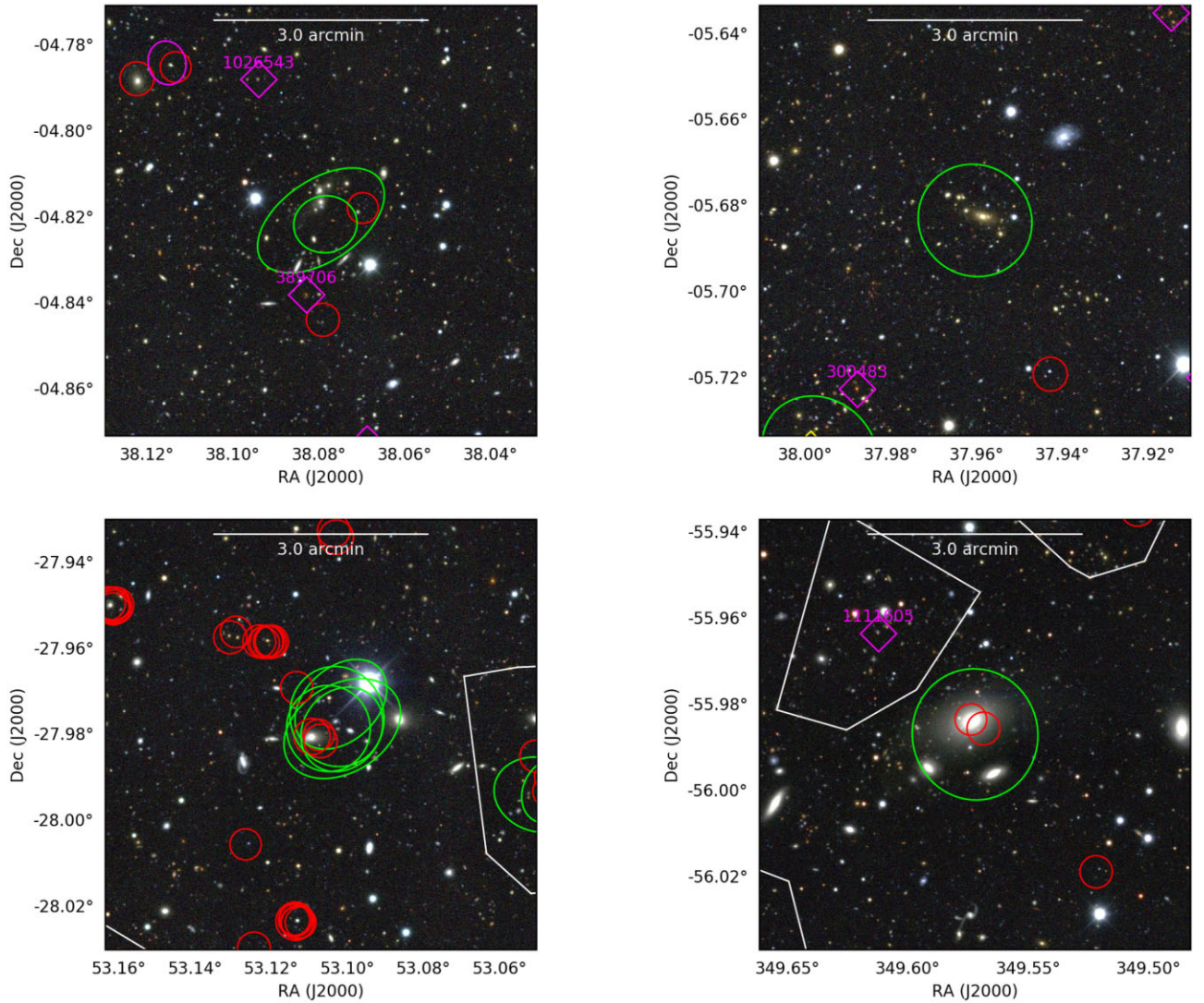## The 4 X-ray Detected Clusters Not Found in redMaPPer Catalogue

Figure A5. The four X-ray detected clusters that are not in the redMaPPer catalogue. Green ellipses represent X-ray detected extended sources. Purple diamonds are centred on redMaPPer clusters. Top Left: From redMaPPer scan-Redshift: 0.2 λ: 15.26 Top Right: From redMaPPer scan-Redshift: 0.34 λ: 9.233 Bottom Left: From redMaPPer scan-Redshift: 0.12 λ: 5.95 Bottom Right: From redMaPPer scan-Redshift: 0.09 λ: 13.93.

[1]*Department of Physics and Astronomy, University of Sussex, Brighton BN1 9QH, UK*

[2]*Astrophysics Research Centre, University of KwaZulu-Natal, Westville Campus, Durban 4041, SA*

[3]*School of Mathematics, Statistics, and Computer Science, University of KwaZulu-Natal, Westville Campus, Durban 4041, SA*

[4]*Kavli Institute for Particle Astrophysics & Cosmology, P. O. Box 2450, Stanford University, Stanford, CA 94305, USA*

[5]*Department of Statistics and Data Sciences, The University of Texas at Austin, Austin, TX 78712, USA*

[6]*AIM, CEA, CNRS, Université Paris-Saclay, Université Paris Diderot, Sorbonne Paris Cité, F-91191 Gif-sur-Yvette, France*

[7]*Santa Cruz Institute for Particle Physics, University of California, Santa Cruz, 1156 High St, Santa Cruz, CA 95064, USA*

[8]*Faculty of Physics, Ludwig-Maximilians-Universität, Scheinerstr. 1, D-81679, Munich, Germany*

[9]*Astrophysics Research Institute, Liverpool John Moores University, Liverpool Science Park, 146 Brownlow Hill, Liverpool L3 5RF, UK*

[10]*Instituto de Astrofísica e Ciências do Espaço, Universidade do Porto, CAUP, Rua das Estrelas, P-4150-762 Porto, Portugal*

[11]*Departamento de Física e Astronomia, Faculdade de Ciências, Universidade do Porto, Rua do Campo Alegre, 687, P-4169-007 Porto, Portugal*

[12]*Institute for Astronomy, University of Edinburgh, Royal Observatory, Blackford Hill, Edinburgh EH9 3HJ, UK*

[13]*Astronomy Department, University of Michigan, Ann Arbor, MI 48109, USA*

[14]*Department of Physics and Astronomy, Uppsala University, SE-751 20 Uppsala, Sweden*

[15]*Department of Physics, Lancaster University, Lancaster LA1 4YB, UK*

[16]*Fermi National Accelerator Laboratory, P. O. Box 500, Batavia, IL 60510, USA*

[17]*Department of Physics, University of Michigan, Ann Arbor, MI 48109, USA*

[18]*Institute of Cosmology and Gravitation, University of Portsmouth, Portsmouth, PO1 3FX, UK*

[19]*Sorbonne Universités, UPMC Univ Paris 06, UMR 7095, Institut d'Astrophysique de Paris, F-75014, Paris, France*

[20]*University Observatory, Faculty of Physics, Ludwig-Maximilians-Universität, Scheinerstr. 1, D-81679 Munich, Germany*

[21]*Department of Physics & Astronomy, University College London, Gower Street, London, WC1E 6BT, UK*

[22]*SLAC National Accelerator Laboratory, Menlo Park, CA 94025, USA*

[23]*Center for Astrophysical Surveys, National Center for Supercomputing Applications, 1205 West Clark St., Urbana, IL 61801, USA*

[24]*Department of Astronomy, University of Illinois at Urbana-Champaign, 1002 W. Green Street, Urbana, IL 61801, USA*

[25]*Institut de Física d'Altes Energies (IFAE), The Barcelona Institute of Science and Technology, Campus UAB, E-08193 Bellaterra, Barcelona, Spain*

[26]*Astronomy Unit, Department of Physics, University of Trieste, via Tiepolo 11, I-34131 Trieste, Italy*

[27]*INAF – Osservatorio Astronomico di Trieste, via G. B. Tiepolo 11, I-34143 Trieste, Italy*

[28]*Institute for Fundamental Physics of the Universe, Via Beirut 2, I-34014 Trieste, Italy*

[29]*Laboratório Interinstitucional de e-Astronomia – LIneA, Rua Gal. José Cristino 77, Rio de Janeiro, RJ - 20921-400, Brazil*

[30]*Hamburger Sternwarte, Universität Hamburg, Gojenbergsweg 112, D-21029 Hamburg, Germany*

[31]*Centro de Investigaciones Energéticas, Medioambientales y Tecnológicas (CIEMAT), Madrid 28040, Spain*

[32]*Department of Physics, IIT Hyderabad, Kandi, Telangana 502285, India*

[33]*Jet Propulsion Laboratory, California Institute of Technology, 4800 Oak Grove Dr, Pasadena, CA 91109, USA*

[34]*Institute of Theoretical Astrophysics, University of Oslo. P.O. Box 1029 Blindern, NO-0315 Oslo, Norway*

[35]*Kavli Institute for Cosmological Physics, University of Chicago, Chicago, IL 60637, USA*

[36]*Instituto de Fisica Teorica UAM/CSIC, Universidad Autonoma de Madrid, E-28049 Madrid, Spain*

[37]*Department of Astronomy, University of Michigan, Ann Arbor, MI 48109, USA*

[38]*School of Mathematics and Physics, University of Queensland, Brisbane, QLD 4072, Australia*

[39]*Center for Cosmology and Astro-Particle Physics, The Ohio State University, Columbus, OH 43210, USA*

[40]*Department of Physics, The Ohio State University, Columbus, OH 43210, USA*

[41]*Center for Astrophysics | Harvard & Smithsonian, 60 Garden Street, Cambridge, MA 02138, USA*

[42]*Australian Astronomical Optics, Macquarie University, North Ryde, NSW 2113, Australia*

[43]*Lowell Observatory, 1400 Mars Hill Rd, Flagstaff, AZ 86001, USA*

[44]*Departamento de Física Matemática, Instituto de Física, Universidade de São Paulo, CP 66318, São Paulo, SP, 05314-970, Brazil*

[45]*George P. and Cynthia Woods Mitchell Institute for Fundamental Physics and Astronomy, and Department of Physics and Astronomy, Texas A&M University, College Station, TX 77843, USA*

[46]*Institució Catalana de Recerca i Estudis Avançats, E-08010 Barcelona, Spain*

[47]*Max Planck Institute for Extraterrestrial Physics, Giessenbachstrasse, D-85748 Garching, Germany*

[48]*Observatório Nacional, Rua Gal. José Cristino 77, Rio de Janeiro, RJ - 20921-400, Brazil*

[49]*Department of Physics, University of Genova and INFN, Via Dodecaneso 33, I-16146, Genova, Italy*

[50]*School of Physics and Astronomy, University of Southampton, Southampton, SO17 1BJ, UK*

[51]*Computer Science and Mathematics Division, Oak Ridge National Laboratory, Oak Ridge, TN 37831, United States*

[52]*Lawrence Berkeley National Laboratory, 1 Cyclotron Road, Berkeley, CA 94720, USA*

[53]*Universitäts-Sternwarte, Fakultät für Physik, Ludwig-Maximilians Universität München, Scheinerstr. 1, D-81679 München, Germany*

This paper has been typeset from a TEX/LATEX file prepared by the author.